

STRONG MOLECULAR HYDROGEN EMISSION AND KINEMATICS OF THE MULTIPHASE GAS IN RADIO GALAXIES WITH FAST JET-DRIVEN OUTFLOWS

P. GUILLARD¹, P. M. OGLE¹, B. H. C. EMONTS², P. N. APPLETON³, R. MORGANTI^{4,5}, C. TADHUNTER⁶, T. OOSTERLOO^{4,5}, D. A. EVANS⁷, AND A. EVANS^{8,9}

Draft version June 28, 2018

ABSTRACT

Observations of ionized and neutral gas outflows in radio-galaxies (RG) suggest that AGN radio jet feedback has a galaxy-scale impact on the host ISM, but it is still unclear how the molecular gas is affected. Thus it is crucial to determine the physical conditions of the molecular gas in powerful RG to understand how radio sources may regulate the star formation in their host galaxies. We present deep *Spitzer IRS* high-resolution spectroscopy of 8 nearby RG that show fast HI outflows. Strikingly, all of these HI-outflow RG have bright H₂ mid-IR lines that cannot be accounted for by UV or X-ray heating. This strongly suggests that the radio jet, which drives the HI outflow, is also responsible for the shock-excitation of the warm H₂ gas. In addition, the warm H₂ gas does not share the kinematics of the ionized/neutral gas. The mid-IR ionized gas lines (with FWHM up to 1250 km s⁻¹ for [NeII]12.8μm) are systematically broader than the H₂ lines, which are resolved by the *IRS* in ≈ 60% of the detected lines (with FWHM up to 900 km s⁻¹). In 5 sources, 3C 236, 3C 293, 3C 459, 4C 12.50 and PKS 1549-79, the [NeII]λ12.8μm line, and to a lesser extent the [NeIII]λ15.5μm and [NeV]λ14.3μm lines, clearly exhibit blue-shifted wings (up to -900 km s⁻¹ with respect to the systemic velocity) that match well the kinematics of the outflowing HI or ionized gas. The H₂ lines do not show these broad wings, except tentative detections in 4C 12.50, 3C 459 and PKS 1549-79. This shows that, contrary to the HI gas, the H₂ gas is inefficiently coupled to the AGN jet-driven outflow of ionized gas. While the dissipation of a small fraction (< 10%) of the jet kinetic power can explain the turbulent heating of the molecular gas, our data show that the bulk of the warm molecular gas is not expelled from these galaxies.

Subject headings: galaxies: jets, galaxies: kinematics and dynamics, galaxies: evolution, galaxies: ISM, shock waves, ISM: general, ISM: jets and outflows, molecular processes, turbulence

1. INTRODUCTION

Active galactic nucleus (AGN) feedback is recognised to have an important effect on galaxy evolution. Widely introduced in numerical simulations of galaxy evolution to clear the circum-nuclear gas and halt the growth of super-massive black holes (Silk & Rees 1998; Di Matteo et al. 2005), this mechanism would explain the correlations found between the BH mass and e.g. the bulge mass (e.g. Ferrarese & Merritt 2000), and prevent the formation of too many massive galaxies in the early universe (e.g. Thomas et al. 2005).

The co-evolution of massive black holes and their host galaxies has been well established observationally in samples at various redshifts (e.g. Tremaine et al. 2002; Alexander et al. 2005). Nevertheless, detailed observations of individual active galaxies in the nearby universe, where physical processes in the central region can be studied in detail, are essential for answering key questions about the role of AGN

in galaxy evolution, such as what is the magnitude of AGN feedback (e.g. gas outflow rates) and what is the main driving mechanism of AGN feedback (e.g. quasar wind, radio jets, circum-nuclear starbursts).

Most of the existing evidence for AGN radio jet feedback on the scales of galaxy bulges comes from observations of outflows of neutral gas (Morganti et al. 2003, 2005b; Emonts et al. 2005; Lehnert et al. 2011) and ionized gas (Nesvadba et al. 2006, 2008; Holt et al. 2008) in radio galaxies. These observations suggest that radio jets are an efficient mechanism to convert the energy output of the AGN into an energy input into the ISM, and that radio sources may regulate gas cooling in early-type galaxies (Best et al. 2005, 2006; Donoso et al. 2009).

One of major open questions about estimating mass outflow rates is whether the ionized and HI gas traces the dominant phase of the wind. Therefore it is crucial to compare the masses and kinematics of each gas phase. It has only very recently been recognized that starburst and AGN-driven winds also include molecular components (e.g. Veilleux et al. 2009; Feruglio et al. 2010; Alatalo et al. 2011). Fischer et al. (2010) and Sturm et al. (2011) reported the discovery of molecular outflows in nearby ULIRGs (e.g. Mrk 231) through the detection of a series of OH and H₂O lines seen in absorption against the bright IR dust continuum with *Herschel*/PACS in the λ78–79 μm and λ119–121 μm ranges. However, estimates of outflow rates from absorption lines suffer from major uncertainties regarding e.g. the geometry, and the degeneracy between covering fractions and column densities. Moreover, most of these sources are composite: the co-existence of a starburst, quasar, and radio source makes it difficult to infer

¹ *Spitzer* Science Center (SSC), California Institute of Technology, Pasadena, USA

² Australia Telescope National Facility, CSIRO, POBox76, Epping NSW, 1710, AUSTRALIA

³ NASA *Herschel* Science Center (NHSC), California Institute of Technology, Pasadena, USA

⁴ Netherlands Foundation for Research in Astronomy, Dwingeloo, The Netherlands

⁵ Kapteyn Astronomical Institute, University of Groningen, The Netherlands

⁶ Department of Physics & Astronomy, University of Sheffield, UK

⁷ Massachusetts Institute of Technology, Kavli Institute for Astrophysics and Space Research, 77 Massachusetts Avenue, Cambridge, MA02139, USA

⁸ University of Virginia, Charlottesville, USA

⁹ National Radio Astronomical Observatory

what is driving the wind. Starbursts (Rupke et al. 2005), radiation pressure from the quasar (Feruglio et al. 2010), and even mechanical interactions with the radio source (Reynolds et al. 2009) have all been proposed.

Spitzer IRS spectroscopy opened a new perspective from which to study the impact of the injection of kinetic energy on the formation of molecular gas and regulation of star formation in nearby radio galaxies. Ogle et al. (2010) found that 30% of a sample of 55 nearby 3C radio galaxies have unusually bright mid-IR line emission from warm (10^{2-3} K) H_2 gas, with weak tracers of star formation (SF) (e.g. PAHs). The H_2 to PAH luminosity ratio is more than 10 times larger than what is expected from UV and X-ray photon heating. We propose that the H_2 luminosity is associated with the dissipation of a small fraction of the mechanical energy of the radio jet (Nesvadba et al. 2010; Ogle et al. 2010). These H_2 -luminous galaxies lie off the Schmidt-Kennicutt relationship, indicating that star-formation may be suppressed relative to nearby normal star-forming galaxies (Nesvadba et al. 2010). Numerical simulations also suggest that radio jets appear to be efficient at injecting kinetic energy into the ISM (e.g. Wagner & Bicknell 2011), possibly inhibiting star formation.

This paper reports on the mid-IR *Spitzer* IRS (Houck et al. 2004) spectroscopy of 8 nearby powerful radio galaxies in which fast (≈ 1000 km s^{-1}) outflows of ionized and neutral gas have been detected (Morganti et al. 2005b). These galaxies are ideal targets to study the impact of AGN feedback on the different phases of the ISM, and in particular on the molecular gas, and thus on star-formation. They present an environment where winds can clearly be associated with the mechanism driving them, namely the radio jet. How is the kinetic energy of the outflow dissipated? Is the molecular gas entrained in the ionized/neutral outflow? If yes, what are the physical processes that control the dynamical coupling between the tenuous gas outflow and the dense molecular gas?

Sect. 2 and 3 present the galaxy sample and details on the data reduction and spectral analysis. Then we discuss spectroscopic diagnostics (sect. 4), focusing on the H_2 gas, and we compare the kinematics of the ionized, HI, and H_2 gas in sect. 5. Sect. 6 discusses the excitation mechanisms and origin of the H_2 gas, and proposes an interpretation of the observed gas heating and kinematics of the multiphase ISM gas of the host galaxy.

2. THE SAMPLE OF HI-OUTFLOW RADIO GALAXIES

Except PKS 1549-79, all of the observed sources are part of the Morganti et al. (2005b) sample. Most of these sources are bright compact radio sources, with sizes ranging from 0.01 to 40 kpc. These HI-outflow objects appear to belong to the minority of powerful radio galaxies ($\approx 35\%$) that show evidence for recent star formation at optical wavelengths (Tadhunter et al. 2011, based on spectral synthesis modelling) and/or mid-IR wavelengths (Dicken et al. 2011, based on PAH detection). Most such objects are compact radio sources (e.g. CSS/GPS/CSO) or have unusually strong compact steep spectrum cores (Tadhunter et al. 2011). The star formation in these objects is probably linked to the presence of an unusually rich ISM in the nuclear regions of the host galaxies, perhaps accreted in gas-rich mergers. In such objects the radio jets are expected to interact particularly strongly with the dense circumnuclear gas. Therefore these are just the type of objects in which we might expect the jets to have a direct impact on the molecular gas.

Some properties of the sample are listed in Table 1. The

stellar masses are derived from the K-band luminosities according to Marconi & Hunt (2003):

$$\log_{10}(M_*) = -2.3 + 1.21 \times \log_{10}(L_K), \quad (1)$$

where M_* is the bulge stellar mass in M_\odot and L_K the K-band luminosity in L_\odot . The unabsorbed 2–10 keV AGN X-ray fluxes are taken from the literature, except 3C 236, 3C 459 and PKS 1549-79 which were unpublished. For 3C 236, we re-processed and extracted the Chandra ACIS spectrum. We find that the spectrum is well fitted with a single power law of photon index 1.67, absorbed by a column of $N_H = 2.3 \times 10^{23}$ cm^{-2} , consistent with the presence of a dust lane close to the nucleus (de Koff et al. 2000). The 3C 459 and PKS 1549-79 X-ray fluxes were provided by P. O’Brien and M. Hardcastle (private communications). The jet kinetic power is estimated from the 178 MHz flux density, according to the formula¹⁰ derived in Punsly (2005).

These galaxies all show very broad (up to 1000 km s^{-1}) HI absorption profiles, with highly blue-shifted HI gas with respect to their optical systemic velocities, which indicates a fast outflow of neutral gas (e.g. Morganti et al. 2003). The associated HI mass outflow rates are up to $\approx 60 M_\odot$ yr^{-1} , up to 2 orders of magnitude higher than the mass outflow of ionized gas (see e.g. Emonts et al. 2005). These outflow rates are estimated from the gas column density, the outflow velocity, and the radius within which the flow originates (see e.g. Heckman 2002, for a review). In some cases, like 3C 305 (Morganti et al. 2005a), IC 5063 (Oosterloo et al. 2000; Morganti et al. 2007) and 3C 293 (Morganti et al. 2003; Emonts et al. 2005), this radius is estimated from high-resolution radio and optical observations, where the outflow is spatially resolved against the radio continuum, and co-spatial with regions where the radio emission in the propagating radio jet is enhanced. For the other sources, the radii are more uncertain. It is assumed that the outflow is coming from the brightest radio continuum region, which in principle provides only a lower limit since the HI absorption can only be traced in regions where the continuum is bright. We checked that these radii are consistent with optical spectroscopy, but note that these radii estimates only provide an order of magnitude. Some of the main radio and HI properties are summarized in Table 2. In sect. 5.4, we discuss in more detail the HI kinematics, and compare them to the kinematics of the molecular and ionized gas phases.

3. SPITZER OBSERVATIONS, DATA REDUCTION AND ANALYSIS

The IRS has two high-resolution modules, short high¹¹ (SH) and long-high¹² (LH), and four low-resolution modules, short-low (SL1 & SL2) and long-low (LL1 & LL2), spanning 5.2–38 μm . In low resolution mode ($\lambda/\Delta\lambda \approx 57-127$), we used publicly available archival data for 7 of the 8 sources. Only PKS 1549-79 was not previously observed at low resolution, hence we observed this source as part of our *Spitzer* Cycle 4 program p40453. At high resolution ($\lambda/\Delta\lambda \approx 600$), we observed 5 sources (3C 236, 3C 305, 3C 459, PKS 1549-79, and IC 5063) as part of our program p40453, and we used archival data for the remaining 3 sources (3C 293, 4C 12.50, and OQ 208) (p30877). The exposure times for each mode are

¹⁰ This formula uses the 151 MHz flux density. When a direct measurement at 150 MHz was not available, we derived it from the 178 MHz measurement (taken from NED) by fitting the measured radio SED with a power-law.

¹¹ $4.7'' \times 11.3''$ slit, observed wavelengths from 9.9 to 19.6 μm

¹² $11.1'' \times 22.3''$ slit, observed wavelengths from 18.7 to 37.2 μm

Table 1
 Properties of HI-outflow radio-galaxies observed with *Spitzer IRS*

Object	RA ^a J2000.0	Dec ^a J2000.0	z^b	D_L^c [Mpc]	K-mag	M_*^d [M_\odot]	$M(H_2)^e$ [M_\odot]	$M(H_2)$ ref.	$L_{24\mu m}^f$ [L_\odot]	$\log L_X^g$ [erg s^{-1}]	$\log L_X$ ref.	$L(H_2)/L_X^h$
3C 236	10 06 01.7	+34 54 10.4	0.1004	449	12.25	7.4E10	< 8E9	(1)	$1.94 \pm 0.15 \text{ E10}$	43.0		0.054
3C 293	13 52 17.8	+31 26 46.5	0.0448	195	10.84	4.6E10	1.5E10	(2)	$6.26 \pm 0.75 \text{ E09}$	42.8	(4)	0.063
3C 305	14 49 21.8	+63 16 15.3	0.0418	178	10.64	4.8E10	2.0E9	(1)	$7.13 \pm 0.45 \text{ E09}$	41.2	(5)	1.78
3C 459	23 16 35.2	+04 05 18.1	0.2199	1046	$5.36 \pm 0.32 \text{ E11}$	43.2		0.13
4C +12.50	13 47 33.4	+12 17 24.2	0.1234	551	12.21	1.3E11	1.5E10	(3)	$1.20 \pm 0.04 \text{ E12}$	43.3	(6)	0.16
IC 5063 lobe	20 52 02.1	-57 04 06.6	0.0113	45.3	8.75	1.6E10	$3.74 \pm 0.08 \text{ E10}$	42.9	(7)	0.008
OQ 208	14 07 00.4	+28 27 14.7	0.0766	337	11.52	5.2E09	1.4E10	(1)	$2.31 \pm 0.03 \text{ E11}$	42.7	(8)	0.08
PKS 1549-79	15 56 58.9	-79 14 04.3	0.1521	699	$1.31 \pm 0.04 \text{ E12}$	44.7		0.005

References. — (1) Ocaña Flaquer et al. (2010); (2) Evans et al. (1999); (3) Evans et al. (2002); (4) Ogle et al. (2010); (5) Massaro et al. (2009); (6) O’Dea et al. (2000); (7) Lutz et al. (2004); (8) Guainazzi et al. (2004)

^a Positions of the sources used for the Spitzer IRS observations. Except for 3C 305, IC 5063 and 4C 12.50, the positions of the radio nuclei are taken from NED (see Sect. 3 for details).

^b Redshift derived from optical line measurements (see references for the systemic velocities in Table 2).

^c Luminosity distance assuming $H_0 = 73 \text{ km s}^{-1} \text{ Mpc}^{-1}$ and $\Omega_m = 0.27$.

^d Stellar mass derived from the K-band luminosity.

^e H_2 gas masses estimated from CO(1-0) measurements. For 4C 12.50, only the H_2 mass in the western lobe is quoted.

^f Rest $24 \mu\text{m}$ luminosity measured with *Spitzer IRS*. We averaged the flux over 23–25 μm , after removal of the [NeV] 24.31 μm when present.

^g Unabsorbed 2–10 keV nuclear X-ray luminosity in erg s^{-1} . For 3C 236 for which we extracted the X-ray spectrum from the Chandra archive (see sect. 6.1). The PKS 1549-79 X-ray flux is from Chandra data (Paul O’Brien, private communication) and agrees with the Suzaku value ($4.5 \times 10^{44} \text{ erg s}^{-1}$). The 3C 459 X-ray flux is from XMM data (Martin Hardcastle, private communication).

^h Ratio of the H_2 line luminosity (summed over the S(0) to S(3) rotational transitions) to the unabsorbed 2–10 keV nuclear X-ray luminosity.

Table 2
 Radio and HI properties of outflow radio-galaxies observed with *Spitzer IRS*

Object	size ^a [kpc]	size ref.	$F_{178\text{MHz}}$ [Jy]	Q_{jet}^b [erg s^{-1}]	τ	$N(\text{HI})$ [10^{21} cm^{-2}]	$M(\text{HI})^c$ [M_\odot]	v_{sys}^d [km s^{-1}]	v_{sys} ref.	v_{out}^e [km s^{-1}]	\dot{M} [$M_\odot \text{ yr}^{-1}$]	radius ^f [kpc]
3C 236	6.0	(1)	15.7	7.6×10^{45}	0.0033	5.0	1.2E8	30129	(9)	750	47.0	0.5
3C 293	5.0	(2,4)	17.1	5.1×10^{45}	0.0038	6.0	1.0E8	13450	(2)	500	56.0	1.0
3C 305	10.0	(3)	13.8	6.2×10^{45}	0.0023	2.0	4.7E7	12550	(7)	250	12.0	1.0
3C 459	39.0	(5)	30.8	2.5×10^{46}	0.0005	0.75	1.8E7	65990	(10)	300	5.5	1.0
4C 12.50	0.15	(6)	4.6	2.5×10^{45}	0.0017	2.6	7.0E6	37027	(10)	600	21.0	0.02–0.2
IC 5063	8.0	(7)	6.3	2.0×10^{45}	0.0120	10.0	2.4E8	3400	(11)	350	35.0	0.4
OQ 208	0.01	(6)	0.12	5.2×10^{43}	0.0057	8.3	2.0E4	22985	(12)	600	1.2	0.01
PKS 1549-79	0.4	(8)	12.6	7.7×10^{45}	0.02	40.0	1.0E8	45628	(10)	250	30.0	0.1–1.0

References. — (1) de Koff et al. (2000); (2) Emonts et al. (2005); (3) Morganti et al. (2005a); (4) Zirbel & Baum (1998); (5) Nilsson et al. (1993); (6) Xiang et al. (2002); (6) Heisler & Vader (1994); (7) Morganti et al. (2005b); (8) Holt et al. (2006); (9) Hill et al. (1996); (10) Holt et al. (2008); (11) Morganti et al. (1998); (12) Marziani et al. (1993)

^a Size of the radio source. Note that for 3C 293, this is the size of the *inner* radio source.

^b Jet cavity kinetic luminosity estimated from the 178 MHz flux (see text, Sect. 2).

^c Mass of HI gas in the outflowing component (within the radius quoted in the table).

^d Systemic velocity of the galaxy (see text for details).

^e Outflow velocity, estimated as half of the full width at zero intensity of the blue-shifted part of the broad HI component.

^f Radius of the HI outflow region. Except for PKS 1549-79, the radii values are from Morganti et al. (2005b).

listed in Table 3, and were chosen to reach a signal-to-noise ratio of at least 10 for the H_2 S(1) 17 μm line.

Even if the outflow of neutral gas is occurring at a kpc-scale distance from the nucleus, this is still spatially unresolved with the IRS in high-resolution mode. However, two sources (3C 305 and IC 5063) exhibit a more extended inner radio structure, and we placed the slit slightly off-nucleus, coincident with a bright peak in the radio continuum, at a distance of 2 arcsec from the core. Note that the core is still included in all of the *IRS* slits. The slit positions are given in Figure 1. 4C 12.50 is a system of two interacting galaxies (Axon et al. 2000), and the SH slit was positioned only to include the western companion. For the other sources, the slits were centred on the nucleus.

3.1. Spitzer data reduction

Table 3
Spitzer IRS observation log

Object	SL	LL	SH	LH
3C 236	13 × 14	5 × 14	4 × 120	10 × 60
3C 305	13 × 14	5 × 14	4 × 120	10 × 60
3C 293	3 × 120	3 × 120	3 × 120	10 × 60
3C 459	16 × 14	2 × 30	4 × 120	10 × 60
4C +12.50	3 × 14	2 × 30	6 × 30	4 × 60
OQ 208	2 × 60	2 × 14	4 × 120	3 × 60
IC 5063 lobe	2 × 14	1 × 30	8 × 30	4 × 60
PKS 1549-79	2 × 60	3 × 30	4 × 120	5 × 60

Note. — Exposure times for the *IRS* modules given as number of cycles × ramp duration in seconds.

The galaxies were observed in staring mode, and placed at two nod positions along the slit (1/3 and 2/3 of the length

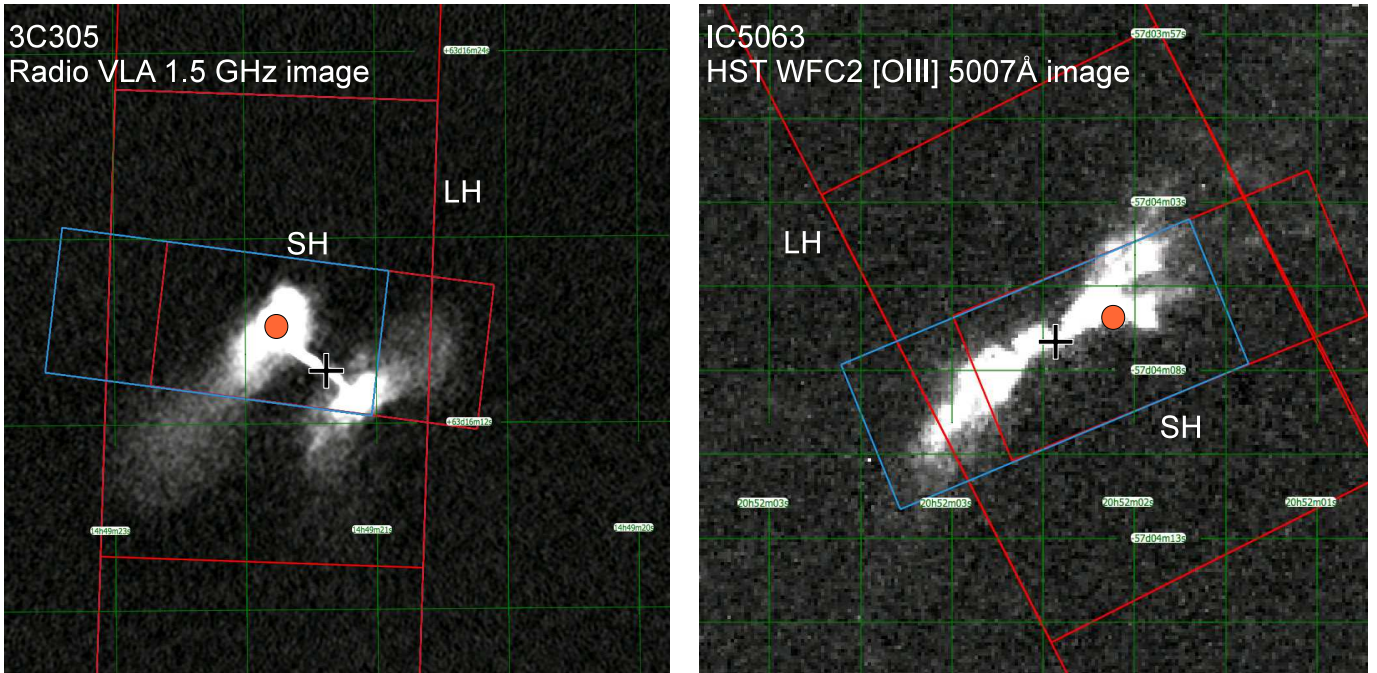


Figure 1. Footprints of the high-resolution IRS slits (SH and LH) for the 3C305 and IC5063 galaxies. For these two sources, the radio observations resolve the HI outflow against the radio jet, at a distance of about 2 arcsec from the nucleus. Therefore, the slits were centred slightly off-nucleus, at the location of the broad, blue-shifted HI absorption associated with the outflow (indicated by the orange circle). The position of the radio core is marked with a green cross.

of the slit). The data were processed by the *Spitzer Science Center* S18.7 pipeline. We started the data reduction from the basic calibrated data products, which include corrections for flat-fielding, stray light and non-linearity of the pixels response. All but one (4C 12.50) galaxies had dedicated sky background (off) observations for all high-resolution modules. When available, the 2D *off* spectra were subtracted from the *on* observation for each nod position. For 4C 12.50, the LH module was used to remove the background emission. For the LH observations, we corrected for the time- and position-dependence of the dark current using the DARK_SETTLE routine¹³.

The cleaning of rogue pixels was performed using the IRSCLEAN routine¹⁴. Rogue pixel masks of the corresponding *IRS* campaigns were used, and a further manual cleaning was done for each nod position and module. The *Spitzer* *IRS* Custom Extractor (SPICE) software was used to extract the one-dimensional SH and LH spectra, with optimal extraction. The individual orders within the high-resolution modules were very well aligned in flux and no scaling was applied between the orders. Then the orders were trimmed (by removing the end of each order, where the response drops) and stitched together. Finally a median combination was used to produce the final stacked spectra.

For all but one source (4C 12.50), the continuum levels of the SH and LH matched and no scaling was necessary. For 4C 12.50, we scaled the SH spectrum by a factor of 1.1 to match the LH module, since it is the most accurate due to its background subtraction.

The 3C236 and 3C305 low-resolution spectra were extracted from spectral maps with the CUBISM¹⁵ software. For the other galaxies, the low-resolution observations were done

in *IRS* staring mode, and the SMART package¹⁶ was used to perform optimal extraction. We checked on 3C 293 that the SPICE and SMART extractions give very similar results.

3.2. Spectral analysis

To measure the fluxes and linewidths of emission lines, we first fitted the spectra with the IDL PAHFIT (Smith et al. 2007) tool, which decomposes the spectra into starlight, thermal blackbody emission (extinguished by a uniform dust screen if specified), resolved PAH features (fitted by Drude profiles), and emission lines. Originally designed to fit low-resolution *Spitzer* *IRS* spectra, we adapted the routine to handle high-resolution data. In particular, we allow the emission lines to be spectrally resolved and we fit them by Gaussian profiles.

We use the PAHFIT decompositions to measure the fluxes of the PAH complexes, and to produce starlight-free and dust-free spectra. Except for OQ 208 and PKS 1549-79, we do not include any extinction in the fit. For OQ 208, 4C 12.50 and PKS 1549-79, we introduced the capability of fitting silicate absorption features at 9.7 and 18 μm . Then we ran PAHFIT a second time to fit accurately the emission lines. We also fitted the lines with Gaussian profiles using the non-linear least-squares IDL fitting routine MPFIT (Markwardt 2009) on the continuum-free spectra. The two methods agree very well and give similar line fluxes (within the uncertainties). We find significant differences (up to a factor of 3 in line flux) when trying to measure the line fluxes in one go with PAHFIT, the many free parameters making the fit inaccurate.

For each of undetected emission lines, we computed the flux of an unresolved Gaussian line with a peak flux equal to twice the rms noise in a 1 μm -wide band centred at the wavelength of the line. We took this flux value as a 2σ upper limit.

We also compute the 24 μm rest-frame fluxes by averaging the *IRS* line-free spectrum over a narrow band (23–25 μm). These narrowband 24 μm fluxes are listed in Table 1.

¹³ <http://irsa.ipac.caltech.edu/data/SPITZER/docs/dataanalysisistools/tools/Chesette>

¹⁴ <http://irsa.ipac.caltech.edu/data/SPITZER/docs/dataanalysisistools/tools/irsclean/>

¹⁵ <http://irsa.ipac.caltech.edu/data/SPITZER/docs/dataanalysisistools/tools/cubism> <http://isc.astro.cornell.edu/IRS/SmartRelease>

4. SPECTROSCOPIC DIAGNOSTICS

The full high-resolution (SH+LH, i.e. observed wavelengths 9.9–37.2 μm) spectra are shown in Figure 2, and the low-resolution spectra are presented on Figure 3. The location of the detected PAH complexes and emission lines are marked on each spectrum. Overall, the spectra are of very good quality, with noise levels expected for such exposure times. Some minor spurious features still remain, in particular in the LH spectra (noisier than the SH), which are due to bad pixels or instrumental artefacts that were not cleaned during the data reduction. In appendix, we provide zooms on the SH wavelengths (Figure 9), and on all individual detected emission lines (Figure 10 and 11).

4.1. Molecular hydrogen

Powerful emission lines from H_2 are detected in all of the 8 high-resolution spectra. The H_2 0-0 S(1) 17 μm and 0-0 S(3) 9.7 μm lines are detected in all radio-galaxies. The pure rotational H_2 line fluxes (or their 2σ upper limits) are listed in Table 4. In some cases, like 3C 236, 3C 293, and 4C 12.50, the H_2 S(1) line dominates the SH spectrum (Figure 9). These H_2 strengths are comparable to those observed in the Ogle et al. (2010) sample of H_2 -bright radio-galaxies, in some galaxy collisions, like Stephan’s Quintet (Cluver et al. 2010) and the Taffy galaxies (Peterson et al. submitted).

To compute the masses of the warm ($\gtrsim 100\text{K}$) H_2 , we follow two different approaches. The first one is similar to that described by Ogle et al. (2010) and consists of assuming a thermal distribution of the H_2 levels. We constructed excitation diagrams, shown on Figure 12, by plotting the logarithm of the column densities of the upper H_2 levels divided by their statistical weights, $\ln(N_{vJ}/g_J)$, against their excitation energies, E_{vJ}/k_B , expressed in K. For a uniform excitation temperature, the values $\ln(N_{vJ}/g_J)$ should fall on a straight line plotted versus E_{vJ}/k_B , with a slope proportional to T_{exc}^{-1} . In a situation of local thermal equilibrium (LTE), the excitation temperature T_{exc} equals that of the gas. We fitted the data with two or three excitation temperature components, although the gas is at a continuous range of temperatures. We constrained the temperature range to be $100 < T < 1500\text{K}$. At each fitting iteration, the statistical weights of the ortho transitions were adjusted to match the LTE value.

The results are given in Table 5, where we list the fitted H_2 excitation temperatures, ortho-to-para ratios, column densities, masses, and total luminosities for each temperature component. The bulk of the warm H_2 is constrained by the lowest temperature component, i.e. by the S(0) and S(1) lines. Thus, if the S(0) line is not detected, we include its upper limit in the fit as a 2σ detection (with 1σ error bar) and quote the model results as upper limits. In all galaxies where the S(0) line is detected, we measure warm H_2 masses, from $\approx 3 \times 10^8 M_\odot$ in 3C 236, up to $\approx 3 \times 10^{10} M_\odot$ in 4C 12.50. Similar extremely large warm H_2 masses were detected in 3C 433 and 3C 436 (Ogle et al. 2010). The H_2 column densities range from $< 4 \times 10^{20}$ to $\approx 2 \times 10^{22} \text{cm}^{-2}$. These column densities depend on the assumed size of the emission region.

The second approach to fit the H_2 line fluxes and derive the H_2 physical parameters is similar to that described in Guillard et al. (2009) and Nesvadba et al. (2010). It assumes that the H_2 emission is powered by the dissipation of mechanical energy in the molecular gas (see sect. 6.1 for a discussion of the H_2 excitation mechanisms). We model this dissipation with magnetic shocks, using the MHD code described

in Flower & Pineau Des Forêts (2010). The gas is heated to a range of post-shock temperatures that depend on the shock velocity, the pre-shock density, and the intensity of the magnetic field (which is perpendicular to the shock propagation). We use a grid of shock models (varying shock speeds) similar to that described in Guillard et al. (2009), at pre-shock densities $n_{\text{H}} = 10^3 \text{cm}^{-3}$ and 10^4cm^{-3} . The initial ortho-to-para ratio is set to 3, and the intensity of the pre-shock magnetic field is 30 μG . The H_2 line fluxes are computed when the post-shock gas has cooled down to a temperature of 100 K. At a given pre-shock density, the shock velocity is the only parameter we allow to vary.

A combination of two shock velocities is required to match the observed H_2 line fluxes. We show the best-fitting shock combination in Figure 13 and 14 for the two pre-shock densities. These fits are not unique, but they provide an estimate of the range of shock velocities and pre-shock densities needed to reproduce the H_2 excitation. This phase-space is well constrained when six or more H_2 lines are detected. The lowest density and shock velocity is required to fit the low-excitation lines S(0) and S(1), which probe the bulk of the warm H_2 mass, whereas the high density and shock velocity is needed to fit the high-excitation lines, above S(4). In reality, the H_2 emission arises from a distribution of densities and shock velocities. With the present data we cannot exclude the presence of very high density gas ($n_{\text{H}} > 10^5 \text{cm}^{-3}$).

As discussed in Guillard et al. (2009), the H_2 masses are derived by multiplying the gas cooling time (down to 100 K) by the gas mass flow (the mass of gas swept by the shock per unit time) required to match the H_2 line fluxes. The shock model parameters, gas cooling times, mass flows, and warm H_2 masses are quoted in Tables 6 and 7. The warm H_2 masses derived from the shock modeling are larger than from the LTE model. This is mainly because of the different values of the H_2 ortho-to-para ratio, and because at $n_{\text{H}} = 10^3 \text{cm}^{-3}$, the S(0) and S(1) lines are not fully thermalized.

4.2. Thermal dust continuum and aromatic features (PAHs)

Our sample reveal two types of spectra, those with a flat thermal dust continuum (3C 236, 3C 293, 3C 305), and those with a steep rising continuum at long wavelengths (3C 459, 4C 12.50, IC 5063, OQ 208, and PKS 1549-79). There is a remarkable similarity between the spectra of 3C 236, 3C 293 and 3C 305 with the 3C 326 radio-galaxy (Ogle et al. 2007), the Stephan’s Quintet (Cluver et al. 2010) and the Taffy galaxies (Peterson et al., submitted), where the dust continuum is very weak compared to emission lines. The narrow-band 24 μm luminosities (see sect. 3.2 and Table 1), measured on the LH spectra, span three orders of magnitude, from $5.4 \times 10^9 L_\odot$ (3C 305) to ULIRG-like luminosities of $1.1 \times 10^{12} L_\odot$ (4C 12.50). For 4C 12.50 and OQ 208, our measurements are in agreement with those of Willett et al. (2010) on low-resolution IRS data.

Emission from aromatic infrared bands attributed to Polycyclic Aromatic Hydrocarbons (PAHs) excited by UV photons are detected in all galaxies. In general, in the high-resolution data, the 11.3 μm band is the most prominent feature. The fluxes of the PAH complexes, given in Table 8, are measured with PAHFIT on the emission line-free spectra (see sect. 3.2), by combining the fluxes of the blended features that contribute to the main complexes (around 8, 11.3, 12.6 and 17 μm).

All of the radio-galaxies have a 11.3 μm PAH to 24 μm

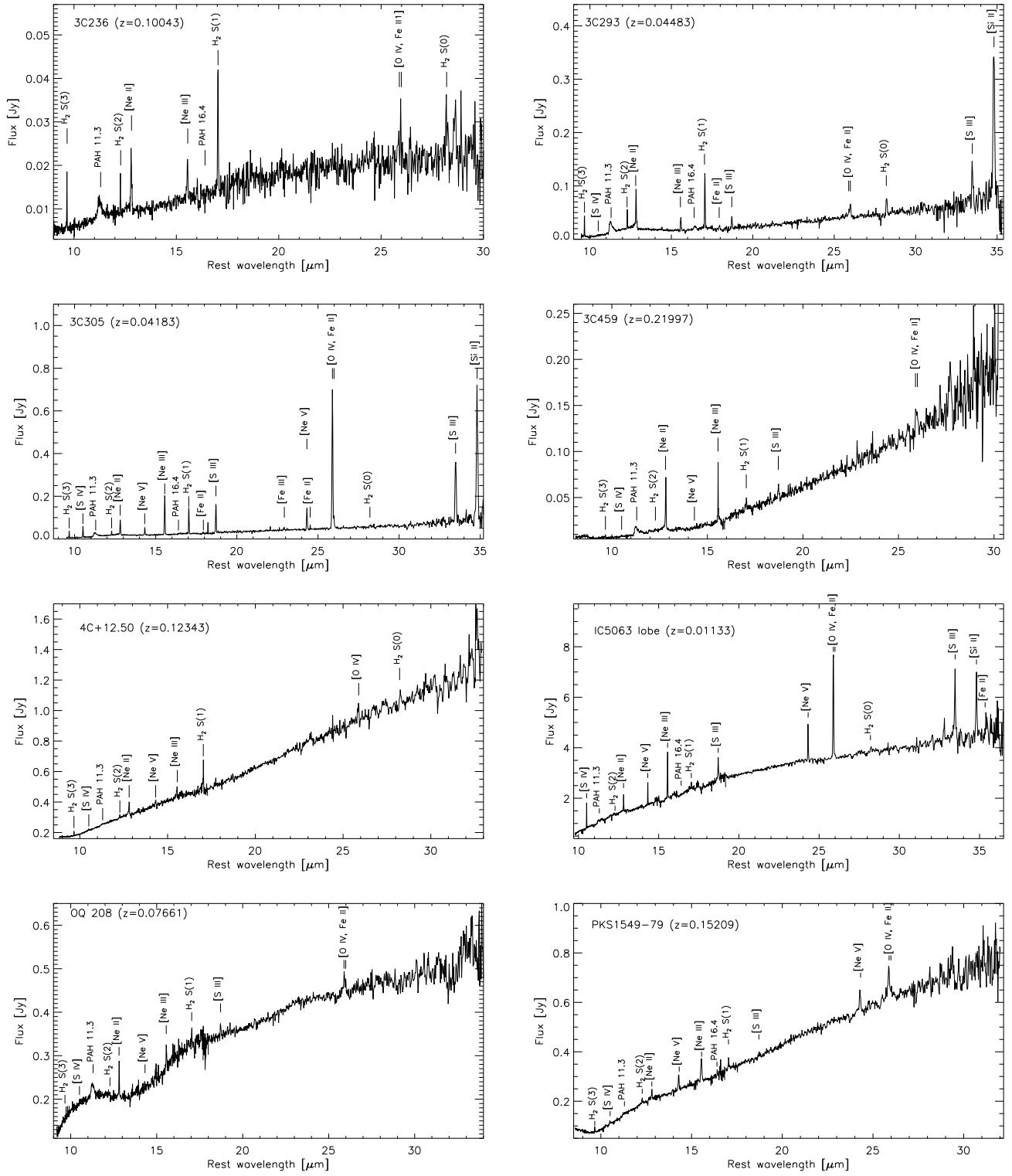


Figure 2. *Spitzer* IRS high-resolution (SH+LH) spectra of the H1-outflow radio-galaxies. The locations of PAH features and emission lines are marked for each object.

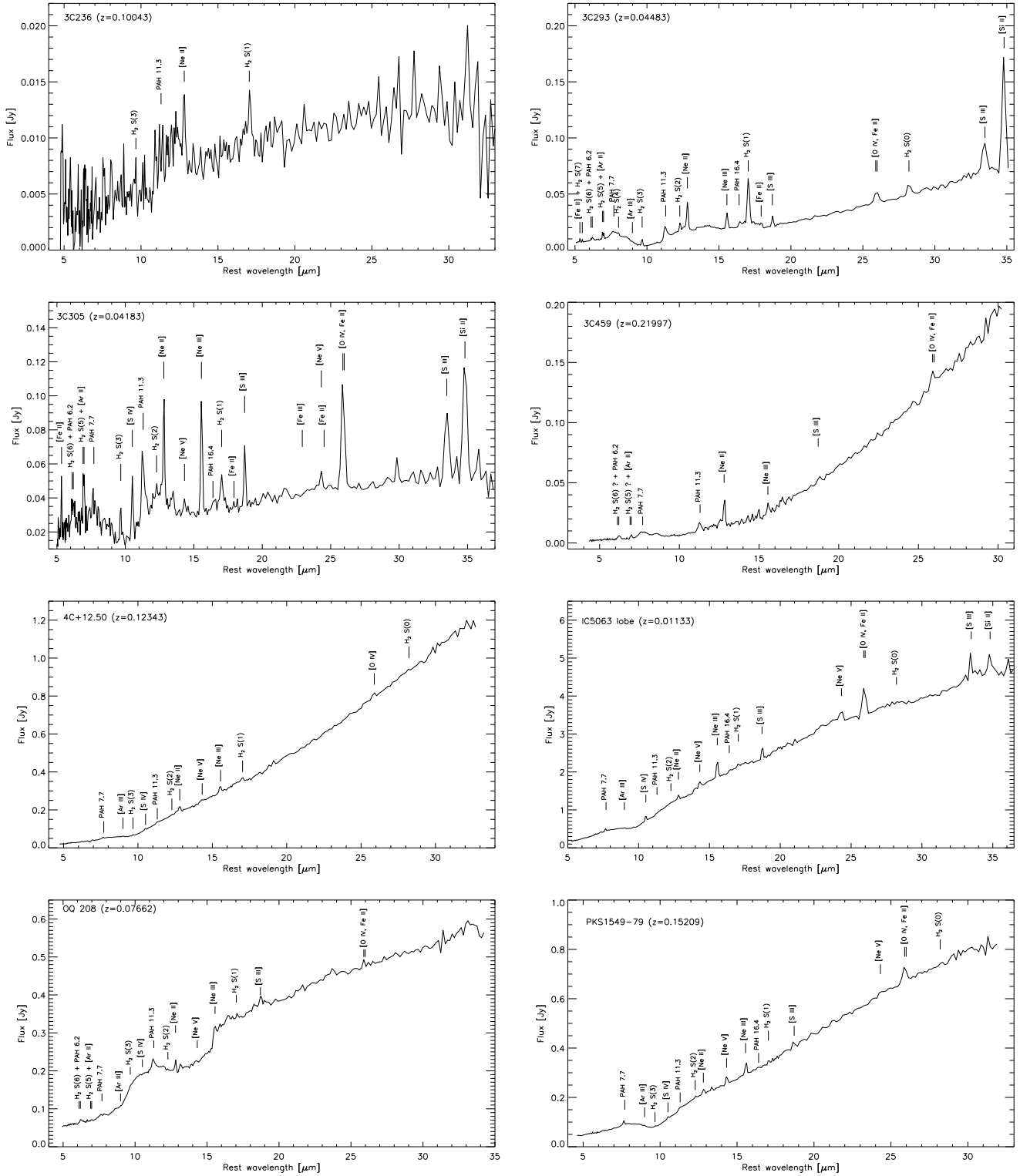


Figure 3. Spitzer IRS low-resolution (SL+LL) spectra of the HI-outflow radio-galaxies. The locations of PAH features and emission lines are marked for each object. The low-resolution spectra for 3C 293, OQ 208 and PKS 1549-79 were already presented by [Ogle et al. \(2010\)](#) and [Willett et al. \(2010\)](#).

Table 4
H₂ line fluxes from HI-outflow radio galaxies

Source	H ₂ S(0) 28.22 μm	H ₂ S(1) 17.03 μm	H ₂ S(2) 12.28 μm	H ₂ S(3) 9.66 μm	H ₂ S(4) 8.03 μm	H ₂ S(5) 6.91 μm	H ₂ S(6) 6.11 μm	H ₂ S(7) 5.51 μm
3C 236	0.20 (0.03)	0.95 (0.07)	0.32 (0.05)	0.64 (0.05)	< 1.04	< 1.10	< 0.23	< 0.31
3C 293	0.79 (0.06)	3.46 (0.29)	1.61 (0.10)	2.50 (0.16)	1.35 (0.13)	2.84 (0.14)	0.65 (0.15)	1.35 (0.19)
3C 305	< 0.31	3.82 (0.42)	0.88 (0.09)	1.89 (0.12)	1.03 (0.39)	2.93 (0.69)	1.83 (0.47)	< 1.40
3C 459	< 0.25	0.55 (0.03)	< 0.36	0.37 (0.02)	< 0.29	< 1.04	< 0.15	< 0.49
4C 12.50	2.31 (0.13)	3.44 (0.39)	0.96 (0.09)	1.44 (0.09)	< 0.72	< 1.41	< 0.93	< 2.63
IC 5063	4.63 (0.24)	10.65 (0.44)	< 1.8	3.86 (0.49)	< 3.12	< 5.10	< 3.38	< 5.20
OQ 208	< 0.38	1.11 (0.09)	< 0.35	0.49 (0.06)	< 0.75	< 4.13	< 2.14	< 2.76
PKS 1549-79	< 0.46	1.45 (0.12)	0.63 (0.08)	0.95 (0.09)	< 1.29	< 2.23	< 1.32	< 3.36

Note. — H₂ mid-IR line fluxes (and 1σ error in parenthesis) in units of 10⁻¹⁷ W m⁻² measured with *Spitzer* IRS. In case of non-detection, the 2σ upper limit is indicated. The H₂ S(0) to S(3) lines are measured in the high-resolution modules (except for IC 5063, where the S(3) line was measured in the SL module because it falls out of the SH wavelength coverage), and the S(4) to S(7) lines in the low-resolution modules. Note that the S(5) and S(6) lines are severely blended with the PAH 6.2 μm and [ArII]λ 6.98 μm features.

Table 5
H₂ excitation diagram fitting for a thermal distribution: results

Source	Size ^a ["]	T(K) ^b [K]	O/P ^c	N(H ₂) ^d [cm ⁻²]	M(H ₂) ^e [M _⊙]	L(H ₂) ^f [L _⊙]
3C 236	3.0	100 (0)	1.587	3.3E+21	1.6E+09 (0.5)	1.5E+07
		241 (27)	2.947	1.9E+20	9.5E+07 (4.0)	8.2E+07
		1045 (80)	3.000	1.5E+18	7.3E+05 (1.8)	1.8E+08
3C 293	4.7	100 (0)	1.587	6.1E+21	1.7E+09 (0.2)	1.2E+07
		285 (14)	2.983	1.9E+20	5.3E+07 (1.1)	7.4E+07
		1048 (47)	3.000	1.9E+18	5.2E+05 (0.8)	1.1E+08
3C 305	4.7	226 (13)	2.922	<4.2E+20	<1.0E+08	5.3E+07
		1253 (93)	3.000	1.3E+18	3.1E+05 (0.5)	1.2E+08
3C 459	1.4	100 (0)	1.587	<2.1E+22	<8.3E+09	1.1E+08
		284 (32)	2.983	1.5E+20	6.1E+07 (3.0)	1.6E+08
		1500 (0)	3.000	1.6E+18	6.3E+05 (1.1)	7.9E+08
4C 12.50	4.7	100 (0)	1.587	2.2E+22	3.8E+10 (0.2)	3.7E+08
		275 (16)	2.978	1.6E+20	2.8E+08 (0.9)	4.4E+08
		1500 (0)	3.000	5.5E+17	9.2E+05 (1.5)	8.3E+08
IC 5063	4.7	100 (0)	1.587	3.9E+22	7.3E+08 (0.9)	4.7E+06
		210 (34)	2.883	1.4E+21	2.6E+07 (1.9)	8.8E+06
		1251 (103)	3.000	3.1E+18	5.9E+04 (2.5)	1.9E+07
OQ 208	2.0	100 (0)	1.587	<9.2E+21	<1.2E+09	1.0E+07
		186 (29)	2.784	2.1E+21	2.8E+08 (2.5)	7.1E+07
		1500 (0)	3.000	2.5E+18	3.4E+05 (0.4)	2.6E+08
PKS 1549-79	1.9	100 (0)	1.587	<2.0E+22	<7.7E+09	8.4E+07
		270 (21)	2.975	5.1E+20	2.0E+08 (0.7)	3.3E+08
		1500 (0)	3.000	3.6E+18	1.4E+06 (0.2)	1.4E+09

^a Assumed size (diameter) of the H₂ emitting source for the calculation of the column densities.

^b Fitted excitation temperature assuming LTE (see text for details).

^c H₂ ortho-to-para ratio (fitted self-consistently to fulfill the LTE approximation).

^d H₂ model column densities.

^e Warm H₂ masses (and 1σ uncertainties) derived from the fit. In case of non-detection of the S(0) line, a 2σ upper limit is quoted.

^f Total H₂ luminosity, summed over all rotational transitions (including those not observed with *Spitzer*, which includes a ≈ 40% correction at 200 K).

luminosity ratio that ranges from $L_{\text{PAH}11.3}/L_{24\mu\text{m}} = 4 \times 10^{-2}$ for 3C 293 to 8×10^{-4} for 4C 12.50, which is similar to the ratios observed in the Ogle et al. (2010) sample of 3C radio-galaxies. This ratio is significantly lower than the SINGS star-forming galaxies, where the median ratio is ≈ 0.1. 3C459, PKS 1549-79 and 4C 12.50 are ULIRGs, but their $L_{\text{PAH}11.3}/L_{24\mu\text{m}}$ ratios are at the lower end of the observed values (≈ 10⁻³). The mid-IR continuum of these radio-galaxies is therefore dominated by dust emission from the accretion disk or synchrotron emission from the jet, but not by star formation. The weakness of the PAH emission relative to the continuum emission is related to the weakness of the stellar UV radiation field (see Ogle et al. 2010, and sect. 6.1 for a dis-

cussion of this claim). Although PAH emission is expected to be diminished because of PAH destruction by hard UV or X-ray radiation close to the AGN Voit (1992), or because of gas suppression close to the nuclei, it is unlikely that their abundances are reduced significantly at galactic scales by AGN effects (Ogle et al. 2010).

Silicate absorption at 9.7 and 18 μm is present in the low-resolution spectra of OQ 208 and 4C 12.50 (Willett et al. 2010), as well as PKS 1549-79. OQ 208 is the only galaxy showing silicate emission (Willett et al. 2010).

4.3. Ionic fine-structure lines

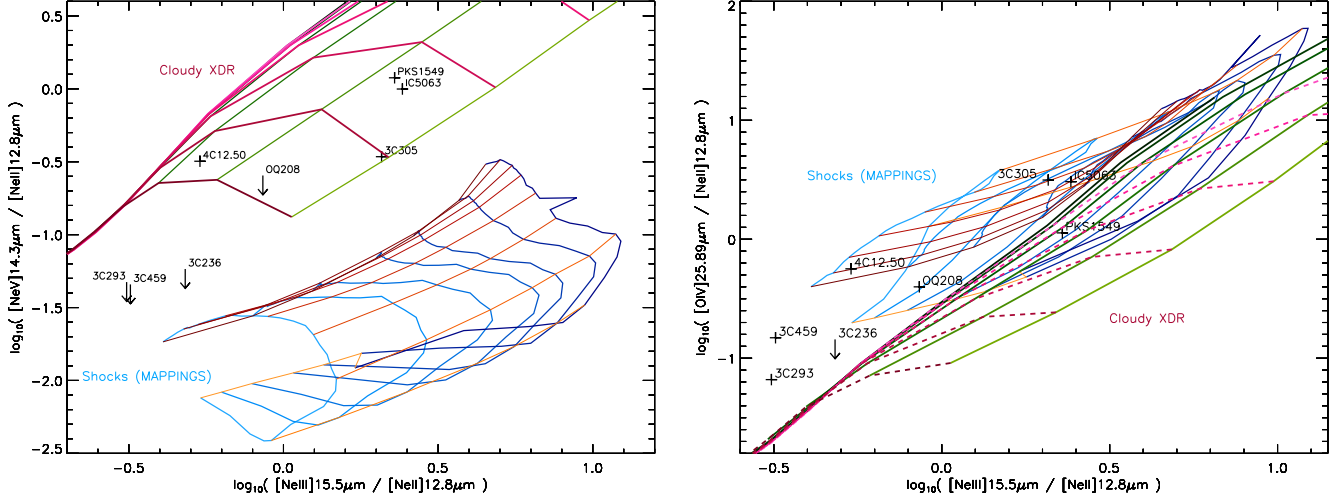


Figure 4. Mid-infrared line diagnostic diagrams for the logarithm of the model line flux ratios [NeV]/[NeII] (left) and [OIV]/[NeII] (right) against [NeIII]/[NeII]. The observed values for the 8 HI-outflow radio-galaxies are compared to shock and photoionization grids of models. The shock model grid is from the Allen et al. (2008) MAPPINGS III shock code for combined precursor and shock models. The gas metallicity is solar and the pre-shock gas density is $n_{\text{H}} = 10 \text{ cm}^{-3}$. The orange lines indicate constant shock velocities, from 200 (light orange) to 1000 km s^{-1} (red), and the blue lines constant magnetic field strengths, from 10^{-3} (light blue) to 100 μG (purple). The deeper the color, the larger is the parameter. The grid of photoionization NLR models was computed with the CLOUDY code (Ferland et al. 1998) with a standard power-law spectral index $\alpha = -1.5$ and varying ionization parameter (green lines, $U_0 = 1 - 10^{-2}$) and density n_{H} (pink lines, $n_{\text{H}} = 10^3 - 10^6 \text{ cm}^{-3}$). On the right plot, since the shock and photoionization models partially overlap, the constant density lines are dashed for clarity.

Table 6

 H₂ fluxes fitted with shock models: results for $n_{\text{H}} = 10^3 \text{ cm}^{-3}$

Source	V_s^a [km s ⁻¹]	Mass flow ^b [M _⊙ yr ⁻¹]	$t_{\text{cool}}(50 \text{ K})^c$ [yrs]	$M(\text{H}_2)^d$ [M _⊙]
3C 236	3	8.0E+04	1.5E+05	1.2E+10
	23	2.4E+03	1.8E+04	4.4E+07
3C 293	5	4.2E+04	8.1E+04	3.4E+09
	40	8.3E+02	7.8E+03	6.4E+06
3C 305	11	7.3E+03	4.4E+04	3.2E+08
	40	3.7E+02	7.8E+03	2.9E+06
3C 459	4	2.6E+05	1.1E+05	2.9E+10
	40	1.8E+03	7.8E+03	1.4E+07
4C 12.50	4	1.1E+06	1.1E+05	1.2E+11
	23	8.6E+03	1.8E+04	1.5E+08
IC 5063	4	1.9E+04	1.1E+05	2.1E+09
	40	7.7E+01	7.8E+03	6.0E+05
OQ 208	5	5.4E+04	8.1E+04	4.3E+09
	40	3.6E+02	7.8E+03	2.8E+06
PKS 1549-79	15	2.3E+04	2.9E+04	6.7E+08
	40	1.9E+03	7.8E+03	1.5E+07

^a Shock velocity.

^b Mass of gas that is traversed by the shock per unit time required to match the observed H₂ line fluxes.

^c Gas cooling time, from the peak post-shock temperature down to 100 K.

^d Warm H₂ masses.

The fluxes of the most commonly detected mid-IR ionized gas lines are listed in Table 9. The [NeII] 12.8 μm and [NeIII] 15.5 μm are detected at high signal to noise ratio (> 6) in all 8 radio-galaxies. The [OIV] 25.9 μm and [FeII] 25.9 μm pair is also very common, with at least one line of the doublet detected in 7/8 galaxies. The high ionization ($E_{\text{ion}} = 97.12 \text{ eV}$) [NeV] 14.32 μm line is detected in half of the sample. Although listed as non-detected by Farrah et al. (2007) and Willett et al. (2010), we securely detect this line in 4C 12.50 at 3.2σ .

Three objects show detections in both [NeV] 14.32 and 24.32 μm lines. The flux ratios of these two lines are consistent with electron densities of $n_e \approx 3 \times 10^3 \text{ cm}^{-3}$ for IC 5063

Table 7

 H₂ fluxes fitted with shock models: results for $n_{\text{H}} = 10^4 \text{ cm}^{-3}$

Source	V_s^a [km s ⁻¹]	Mass flow ^b [M _⊙ yr ⁻¹]	$t_{\text{cool}}(50 \text{ K})^c$ [yrs]	$M(\text{H}_2)^d$ [M _⊙]
3C 236	4	2.2E+05	2.5E+04	5.6E+09
	29	2.8E+03	1.8E+03	5.0E+06
3C 293	8	4.0E+04	1.1E+04	4.4E+08
	29	1.5E+03	1.8E+03	2.7E+06
3C 305	5	5.5E+04	1.8E+04	1.0E+09
	32	1.3E+03	1.5E+03	1.9E+06
3C 459	8	8.3E+04	1.1E+04	9.2E+08
	36	6.2E+03	1.2E+03	7.5E+06
4C 12.50	4	1.8E+06	2.5E+04	4.4E+10
	13	3.2E+04	5.3E+03	1.7E+08
IC 5063	4	3.1E+04	2.5E+04	7.8E+08
	38	1.5E+02	1.1E+03	1.6E+05
OQ 208	3	1.6E+05	3.7E+04	5.7E+09
	40	1.6E+03	1.0E+03	1.7E+06
PKS 1549-79	8	1.7E+05	1.1E+04	1.8E+09
	40	1.1E+04	1.0E+03	1.2E+07

^a Shock velocity.

^b Mass of gas that is traversed by the shock per unit time required to match the observed H₂ line fluxes.

^c Gas cooling time, from the peak post-shock temperature down to 100 K.

^d Warm H₂ masses.

and PKS 1549-79¹⁷, and $n_e < 10^3 \text{ cm}^{-3}$ for 3C 305 (see e.g. Figure 3 of Alexander et al. 1999). These densities are below the critical densities of both lines (see also Dudik et al. 2009). Using the [SIII] 18.71 and 33.48 μm line ratios, we find $n_e \approx 2 \times 10^2 \text{ cm}^{-3}$ for 3C 305 and $n_e \approx 3 \times 10^3 \text{ cm}^{-3}$ for IC 5063. The Neon and Sulfur line ratios give consistent estimates of electron densities, although star-forming regions may contribute to the [SIII] line emission, whereas the [NeV] line is principally emitted by AGN-heated regions.

Some more unusual lines, rarely seen in AGN, and that are not listed in Table 9, are detected in the high-quality spec-

¹⁷ Holt et al. (2006) derive $n_e \approx 430 \text{ cm}^{-3}$ for the NLR gas using the [SII](6731/6717Å) line ratio. Holt et al. (2011) derive $n_e = 3 \times 10^3 \text{ cm}^{-3}$ for 4C 12.50 using a more sophisticated technique.

Table 8
Fluxes of the main PAH complexes from HI-outflow radio galaxies

Source	PAH 6.2 μm	PAH 7.7 μm	PAH 11.3 μm	PAH 12.6 μm	PAH 17 μm
3C 236	< 2.5	< 4.5	3.7 (0.1)	3.8 (1.2)	3.2 (1.3)
3C 293	11.1 (0.6)	55.7 (2.5)	21.5 (0.6)	10.4 (0.4)	25.6 (3.2)
3C 305	15.1 (3.4)	63.1 (8.3)	19.2 (0.1)	16.1 (0.2)	11.2 (2.6)
3C 459	7.2 (1.3)	22.5 (1.3)	9.9 (0.2)	9.7 (0.2)	5.7 (0.3)
4C 12.50	9.8 (2.3)	38.3 (1.6)	10.2 (0.2)	18.1 (0.4)	< 9.5
IC 5063	< 43	189 (1.9)	104.9 (2.6)	230.6 (0.8)	53.3 (6.7)
OQ 208	40.8 (2.9)	51.5 (1.4)	55.3 (2.8)	< 61	101 (8)
PKS 1549-79	25 (3.3)	187 (5.3)	37.4 (0.3)	31.7 (0.7)	4.8 (0.6)

Note. — PAH fluxes (and 1σ error in parentheses) in units of $10^{-17} \text{ W m}^{-2}$ measured with *Spitzer* IRS. In case of non-detection, the 2σ upper limit is indicated.

Table 9
Fine-structure line fluxes in HI-outflow radio-galaxies

Object	[ArII] 6.98 μm	[ArIII] 8.99 μm	[SIV] 10.51 μm	[NeII] 12.81 μm	[NeIII] 15.55 μm	[SIII] 18.71 μm	[OIV] 25.89 μm	[FeII] 25.99 μm	[SiII] 33.48 μm	[SiIII] 34.81 μm
3C 236	< 1.6	< 1.9	< 0.13	0.92 (0.06)	0.44 (0.03)	< 0.14	< 0.14	< 0.13	< 0.09	... ^a
3C 293	2.6 (0.3)	0.70 (0.12)	< 0.18	4.07 (0.29)	1.27 (0.09)	< 0.42	0.27 (0.02)	0.57 (0.05)	1.32 (0.12)	5.55 (0.48)
3C 305	2.8 (0.4)	< 1.5	3.21 (0.24)	4.15 (0.29)	8.62 (0.59)	4.11 (0.33)	13.07 (1.15)	0.90 (0.07)	5.14 (0.46)	11.24 (0.97)
3C 459	1.0 (0.1)	< 0.15	0.11 (0.01)	3.11 (0.22)	1.00 (0.07)	0.39 (0.03)	0.46 (0.04)	0.58 (0.05)	... ^a	... ^a
4C 12.50	< 2.7	2.4 (0.2)	< 0.7	5.45 (0.39)	2.99 (0.21)	< 0.83	2.88 (0.25)	< 0.21	... ^a	... ^a
IC 5063	4.4 (0.2)	9.5 (0.3)	37.60 (3.05)	22.83 (1.62)	56.85 (3.92)	23.88 (1.93)	69.32 (6.10)	3.97 (0.33)	31.89 (2.68)	28.3 (1.1) ^b
OQ 208	1.2 (0.2)	< 1.8	< 1.6	3.33 (0.24)	2.60 (0.18)	< 1.12	1.21 (0.11)	0.45 (0.04)	< 1.4 ^b	... ^a
PKS 1549-79	3.2 (0.3)	3.3 (0.2)	1.45 (0.12)	2.20 (0.17)	5.45 (0.39)	< 0.6	3.11 (0.27)	< 0.8	... ^a	... ^a

Note. — Ionic line fluxes (and 1σ error in parentheses) in units of $10^{-17} \text{ W m}^{-2}$ measured with *Spitzer* IRS. In case of non-detections, a 2σ upper limit is quoted. The [ArII] and [ArIII] lines are measured in the low-resolution modules. All the other lines are measured in the high-resolution modules, except some of the [SIII] and [SiII] lines marked with a (*b*).

^a Observed wavelength not visible in the IRS range.

^b Measured on the low-resolution LL module.

Table 10
High-ionization forbidden emission lines

Object	[NeVI] λ 7.65 μm	[NeV] λ 14.32 μm	[NeV] λ 24.32 μm
3C 236	< 1.6	< 0.06	< 0.06
3C 293	< 0.53	< 0.21	< 0.17
3C 305	0.92 (0.32)	1.42 (0.12)	1.87 (0.15)
3C 459	< 0.29	< 0.16	< 0.14
4C 12.50	2.66 (0.18)	1.68 (0.22)	< 1.1
IC 5063	3.51 (0.12)	22.70 (1.86)	17.41 (1.43)
OQ 208	< 1.2	< 0.8	< 0.2
PKS 1549-79	3.29 (0.21)	3.35 (0.27)	2.21 (0.18)

Note. — Line fluxes (and 1σ error in parentheses) in units of $10^{-17} \text{ W m}^{-2}$ measured with *Spitzer* IRS. In case of non-detection, a 2σ upper limit is quoted. The [NeVI] λ 7.65 μm line is measured in the SL module. The other lines are measured in the high-resolution modules.

trum of 3C 305. The low-ionization ($E_{\text{ion}} = 7.9 \text{ eV}$) [FeII] 17.94, 24.52, and 25.99 μm lines are present, as well as the [FeIII] 22.93 μm ($E_{\text{ion}} = 16.19 \text{ eV}$). The [ArV] 13.10 μm line is also weakly detected (see the SH spectrum on Figure 9).

In such objects, the excitation of the fine-structure lines can arise from photo-ionization by the AGN (e.g. Veilleux & Osterbrock 1987; Meijerink et al. 2007) or by shocks (e.g. Dopita & Sutherland 1996). In practice, distinguishing between the two excitation mechanisms is difficult, since the line flux ratios can be differentially affected by the structure (homogeneous or clumpy) of the emitting gas, and since the model predictions for fine-structure line flux ratios are degenerate for both excitation mechanisms (see also Groves et al. 2006).

In Sect. 6.1, we will show that the warm H_2 emission is

likely powered by shocks. Is it also the case for the observed ionized line emission? In Figure 4, we compare the observed values of three fine-structure line flux ratios to the predictions of shock and photo-ionization models. The grid of fast ($\gtrsim 200 \text{ km s}^{-1}$) radiative shocks is from Allen et al. (2008). The pre-shock gas density is $n_{\text{H}} = 10 \text{ cm}^{-3}$. Note that augmenting the density by a factor 10 reduces these line flux ratios by a factor 2–3 on average, thus shifting the models to the bottom left of Figure 4 by 0.3–0.5 dex. The photo-ionization models are computed with the CLOUDY code (Ferland et al. 1998), with a setup updated from the narrow line region (NLR) models presented in Ferland & Netzer (1983). We used a dusty gas slab model at constant pressure, a power-law ionizing continuum with $f_{\nu} \propto \nu^{-1.5}$ and no cut-off or extinction. We varied the hydrogen density of the gas from 10^3 to 10^6 cm^{-3} and the ionization parameter¹⁸ from $U_0 = 10^{-2}$ to 1. Note that these models are simplistic: they do not include geometrical and inhomogeneity effects, as well as metallicity differences (assumed to be solar here). A detailed model of the mid-IR emission of these sources is beyond the scope of this paper.

The [NeIII] 15.55 μm / [NeII] 12.8 μm line flux ratios are in the range of 0.3–2.4, much higher than those observed in pure starburst galaxies (0.05–0.2, e.g. Bernard-Salas et al. 2009). These ratios are consistent with shock models for $v < 250 \text{ km s}^{-1}$ and $n_{\text{H}} < 10^2 \text{ cm}^{-3}$, the higher values of [NeIII] / [NeII] ≈ 2 requiring very low gas densities ($n_{\text{H}} < 1 \text{ cm}^{-3}$).

¹⁸ $U_0 = S_*/(n_e c)$ is a direct measure of the ionization state of the gas, where S_* is the flux of ionizing photons, n_e the electron density at the inner face of the slab of gas, and c the speed of light.

The range of observed [NeIII]/[NeII] ratios is also consistent with photo-ionization models. This ratio is weakly dependent on the ionization state of the gas, and sensitive to the gas density. The observed [NeIII]/[NeII] ratios require $n_{\text{H}} > 10^3 \text{ cm}^{-3}$.

[NeV] 14.32 μm being a high ionization potential line ($E_{\text{ion}} = 97.1 \text{ eV}$), the [NeV] 14.32/[NeII] 12.8 line ratio is very sensitive to the ionization conditions, and therefore a strong indicator of the AGN contribution (e.g. [Sturm et al. 2002](#)). The shock radiative precursor, which ionizes the gas ahead of the shock front by UV and soft X-ray photons, adds an emission component of a highly ionized gas. However, for the sources containing a powerful AGN, the high values of the observed [NeV]/[NeII] ratios (left panel in [Figure 4](#)) rule out shocks as the dominant excitation mechanism to power the [NeV] luminosity. The [NeV] line primarily arises from photo-ionization of the gas by the AGN. According to this grid of CLOUDY models, the observed [NeV] 14.32/[NeII] 12.8 ratios are consistent with $n_{\text{H}} > 10^3 \text{ cm}^{-3}$ and $U_0 < 0.1$.

The right panel in [Figure 4](#) uses the lower ionization ($E_{\text{ion}} = 54.93 \text{ eV}$) [OIV] 25.89 μm line. In this case, the shock and photo-ionization model grids cover similar regions of the diagram, making it difficult to distinguish between the two excitation mechanisms. The observed mid-IR line ratios are both consistent with high-velocity shocks ($v > 200 \text{ km s}^{-1}$) and photo-ionization, with a preference for shocks at low values of [NeIII]/[NeII]. Some sources (3C 459, 3C 293 and 3C 236) require higher pre-shock densities ($n_{\text{H}} = 10^2 - 10^3 \text{ cm}^{-3}$) to be consistent with shock models.

5. KINEMATICS OF THE MULTIPHASE GAS

In this section we describe and compare the kinematics of the mid-IR H_2 and ionized gas lines (from the IRS data and optical data from the literature) to the kinematics of the outflowing HI gas.

5.1. Analysis of the line profiles

We fitted all the mid-IR lines with Gaussians on the dust-free high-resolution spectra (sect. 3.2). This allows us to carefully extract line profiles, especially when those are located close to underlying PAH structure, as it is the case for the [NeII] 12.8 μm line for instance. We pay a special attention to the fitting of the [NeII] by checking that the PAH 12.6 μm has been correctly removed by the PAHFIT modelling, since the PAH features at 12.62 and 12.69 μm ([Hony et al. 2001](#)) may contribute to an apparent blue-shifted wing of the line. We validated our subtraction method by simulating the presence of an artificial Lorentzian complex in the 12.6–12.9 μm range of intensity compatible with the observed PAH 6.2 and 7.7 μm features. We find that the strength of the simulated 12.6 μm feature measured with PAHFIT is at least a factor of 5 smaller than the strength of the [NeII] blue wing. In addition, the strength of the 12.7 μm PAH complex correlates with the 6.2 μm feature, which is another indication that our measurement of the 12.7 μm PAH complex is correct.

[Figures 10 and 11](#) show a detailed view of the individual lines. The blended lines, like [OIV] $\lambda 25.89$ and [FeII] $\lambda 25.99$, and the lines exhibiting wings (see sect. 5.4) were fitted with a sum of two Gaussian components.

We assume a Gaussian decomposition of the instrumental profile (shown on each of the lines in [Figures 10 and 11](#)), and we derive the intrinsic linewidth (FWHM w_i in km s^{-1}) from

Table 11
Intrinsic H_2 linewidths in HI-outflow radio-galaxies

Object	$\text{H}_2 \text{ S}(0)$ 28.22 μm	$\text{H}_2 \text{ S}(1)$ 17.03 μm	$\text{H}_2 \text{ S}(2)$ 12.28 μm	$\text{H}_2 \text{ S}(3)$ 9.66 μm
3C 236	< 500	548 (59)	< 500	< 500
3C 293	743 (79)	485 (54)	524 (63)	586 (68)
3C 305	...	482 (54)	525 (63)	566 (66)
3C 459	...	432 (50) ^a	...	751 (81)
4C 12.50	906 (91)	< 500 ^a	529 (63)	< 500
IC 5063	709 (76)	721 (71)	< 500	...
OQ 208	...	< 500
PKS 1549-79	...	585 (62) ^a	< 500	< 500

Note. — H_2 FWHM in units of km s^{-1} measured by single Gaussian fitting. A Gaussian decomposition from the instrument profile is assumed to derive the intrinsic linewidths (w_i , see sect. 5.1 for details).

^a 3C 459, 4C 12.50 and PKS 1549-79 possibly exhibit a blue wing in the $\text{H}_2 \text{ S}(1)$ line, which is not included in the quoted linewidth here because this detection is marginal.

$w_i = (w_m^2 - w_{\text{IRS}}^2)^{1/2}$, where w_m is the FWHM in km s^{-1} directly measured on the observed spectrum, and $w_{\text{IRS}} = c/\mathcal{R}$ is the velocity resolution of the IRS. c is the speed of light, and $\mathcal{R} = 600 \pm 72$ is the spectral resolution of the high-resolution module, corresponding to $w_{\text{IRS}} = 500 \pm 60 \text{ km s}^{-1}$. Measurements of calibration targets indicate that the resolution of the high-resolution module of the IRS is constant over its wavelength coverage ([Dasyra et al. 2008](#)). The error on w_m is computed as $\epsilon_m = (\epsilon_f^2 + \epsilon_{\text{IRS}}^2)^{1/2}$, where $\epsilon_{\text{IRS}} = 60 \text{ km s}^{-1}$ is the error on the instrumental resolution and ϵ_f the error of the measurement, estimated from two Gaussian fits of the line profile, one with the upper flux values (adding flux uncertainties), one with the lower values (subtracting uncertainties). A line is considered resolved when $w_m - \epsilon_m > w_{\text{IRS}} + \epsilon_{\text{IRS}} = 560 \text{ km s}^{-1}$. Unresolved lines are assigned a conservative upper limit of 500 km s^{-1} on their intrinsic linewidths.

5.2. Warm H_2 gas

The intrinsic linewidths (w_i) of the H_2 rotational lines are listed in [Table 11](#). According to the criterion defined above, more than 60% of the detected H_2 lines are resolved by the *Spitzer* IRS, with FWHM up to $\approx 900 \text{ km s}^{-1}$. All the sources, except OQ 208, have at least one broad H_2 line with intrinsic FWHM $> 430 \text{ km s}^{-1}$. 3C 293, 3C 305, 3C 459, 4C 12.50, and IC 5063 show two or more resolved H_2 lines. These results show that the warm H_2 gas is very turbulent in most of the sources. As we will show in sect. 6.2, a fraction of the warm H_2 emission is at velocities larger than the escape velocity.

Three of the sources, 3C 459, 4C 12.50 and PKS 1549-79 exhibit asymmetric H_2 line profiles, with blue-shifted wings ([Figures 6, 10 and 11](#)). However, the detection of these wings is tentative, at a 2.5–2.8 σ significance for the S(1) line, and even weaker for the S(2) and S(3) lines. Therefore we do not attempt to fit these wings, and we do not include them in the FWHM quoted in [Table 11](#). Deeper observations at higher spectral resolution are needed to confirm the blue-shifted H_2 emission and measure what fraction of the the warm H_2 gas is participating to the outflow, and to derive the outflow parameters (warm H_2 mass in the outflowing component, mass outflow rate, etc.).

5.3. Ionized gas

[Table 12](#) lists the intrinsic linewidths of the fine-structure lines. Remarkably, the [NeII] 12.8 μm and [NeIII] 15.5 μm

Table 12
Intrinsic linewidths of ionic fine-structure lines in HI-outflow radio-galaxies

Object	[SIV] 10.51 μm	[NeII] 12.81 μm	[NeV] 14.32 μm	[NeIII] 15.55 μm	[SIII] 18.71 μm	[NeV] 24.32 μm	[OIV] 25.89 μm	[FeII] 25.99 μm	[SIII] 33.48 μm	[SiII] 34.81 μm
3C 236	...	1239 (109)	...	875 (86)
3C 293	...	861 (84)	...	877 (86)	723 (83)	595 (70)	...	779 (85)
3C 305	709 (79)	864 (84)	611 (72)	817 (82)	543 (64)	< 500	488 (62)	< 500	565 (67)	746 (82)
3C 459	573 (68)	775 (77)	...	< 500	794 (125)	...	< 500	789 (86)
4C 12.50	...	1033 (95)	852 (92)	838 (83)	767 (87)	< 500
IC 5063	< 500	408 (49)	< 500	< 500	632 (71)	< 500	< 500	661 (75)	< 500	...
OQ 208	...	< 500	...	895 (87)	781 (89)	< 500
PKS 1549-79	1355 (132)	848 (83)	967 (89)	1233 (105)	...	834 (89)	857 (95)

Note. — FWHM in units of km s^{-1} measured by single Gaussian fitting. A Gaussian decomposition from the instrument profile is assumed to derive the intrinsic linewidths (w_i , see sect. 5.1 for details).

lines, the brightest among detected fine-structure lines, are spectrally resolved in 6/8 objects, with intrinsic FWHM up to $\approx 1250 \text{ km s}^{-1}$ (velocity dispersions up to $\approx 540 \text{ km s}^{-1}$).

In five sources (3C 236, 3C 293, 3C 459, 4C 12.50 and PKS 1549) the [NeII], and to a lesser extent [NeIII] and [NeV], line profiles are *asymmetric*. We securely detect blue-shifted (and in some cases red-shifted) wings, up to 3000 km s^{-1} wide, underlying a stronger and narrower peak component centred very close to the optical systemic velocity. As explained in sect. 5.1, we carefully checked that the [NeII]12.8 μm line wings cannot be ascribed to an underlying PAH spectral feature. This result is confirmed by the fact that in most cases the [NeIII]15.5 μm line profile, though noisier but located in a PAH-free part of the spectrum, is consistent with the [NeII]12.8 μm line profile. The kinematic properties of the broad [NeII]12.8 μm features are listed in Table 13. Such wings in the Neon lines have been reported in 4C 12.50 (and in other ULIRGs) by Spoon & Holt (2009).

To characterize the asymmetry and study the kinematics of the outflowing ionized gas, we decomposed the asymmetric line profiles into two Gaussian components, which provides a satisfactory fit. The resulting fit and the broad component are shown on Figures 10 and 11. The detailed results of the fits are listed in Table 13. The intrinsic FWHM of the broad [NeII]12.8 μm components range from $\approx 730 \text{ km s}^{-1}$ (PKS 1549-79) to $\approx 2300 \text{ km s}^{-1}$ (3C 293). In three sources (3C 459, 4C 12.50, and PKS 1549-79), the broad component is clearly blue-shifted with respect to the systemic velocity, with velocity shifts up to $\approx 800 \text{ km s}^{-1}$. For 3C 236, the entire [NeII]12.8 μm line and the broad HI absorption profile are redshifted by $\approx 500 \text{ km s}^{-1}$ with respect to systemic, whereas the H_2 line is centred on the systemic velocity. This is a clear case where a large fraction of the ionized and HI gas is in an outflow, but the H_2 gas is not.

5.4. HI gas

In this section we use the WSRT HI absorption profiles (Morganti et al. 2005b) to quantify the kinematics and energetics of the HI gas. We recall that this HI absorption, detected against the radio continuum, is spatially unresolved, except for IC 5063 and 3C 305. The profiles all exhibit a deep and narrow (FWHM < 200 km s^{-1}) component that traces quiescent gas (likely located in a large scale disk), plus shallow and broad components (with FWHM up to 970 km s^{-1}), mostly blueshifted, that indicate outflowing gas (e.g. Morganti et al. 2003). Two or three Gaussians were necessary to accurately fit the profiles (see Figure 15). The Gaussian fitting parameters and energetics of the HI gas are summarized in Table 14.

At each given velocity, the optical depth (τ) is calculated from $e^{-\tau} = 1 - S_{\text{abs}}/S_{\text{cont}}$, where S_{abs} is the absorption flux and S_{cont} is the underlying radio continuum flux. Then, the HI column density is derived from:

$$\frac{N_{\text{HI}}}{10^{21} \text{ cm}^{-2}} = 1.822 \times \frac{T_{\text{spin}}}{10^3 \text{ K}} \int \tau(v) dv, \quad (2)$$

where v is the velocity and T_{spin} is the spin temperature of the HI gas, assumed to be 1000 K, given that the HI gas is heated by X-ray photons and shocks (see e.g. Bahcall & Ekers 1969; Maloney et al. 1996). Note that this value of T_{spin} is an order of magnitude, and could well be within a $10^2 - 10^4 \text{ K}$ range. The mass of HI gas is derived from N_{HI} and the size of the HI absorption region (see sect. 2 and Table 2).

The turbulent kinetic energy of the HI gas (associated with the velocity dispersion of the gas) is estimated from $E_{\text{kin}}^{(\text{turb})} = 3/2 M_{\text{HI}} \sigma_{\text{HI}}^2$, where $\sigma_{\text{HI}} = \text{FWHM}/2.36$ is the velocity dispersion of the HI gas. The factor of 3 in $E_{\text{kin}}^{(\text{turb})}$ takes into account the three dimensions.

The bulk (radial) mechanical energy of the entrained gas in the outflow is calculated directly from the broad HI profile (after subtraction of the narrow component) by integrating the following quantity relative to the systemic velocity (v_{sys}):

$$\frac{L_{\text{kin}}^{\text{bulk}}}{L_{\odot}} = 1.23 \text{E}4 \frac{r}{1 \text{ kpc}} \frac{T_{\text{spin}}}{10^3 \text{ K}} \int \ln \frac{S_{\text{cont}}}{S_{\text{cont}} - S_{\text{abs}}} \left(\frac{v - v_{\text{sys}}}{10^3 \text{ km/s}} \right)^2 \frac{dv}{1 \text{ km/s}}, \quad (3)$$

where r is the HI outflow radius (see Table 2 and Morganti et al. 2005b).

For comparison, one can assume an outflow with a constant velocity and mass flow \dot{M} , and derive the energy loss rate as (Heckman 2002):

$$\dot{E} = 8.1 \times 10^8 C_f \frac{\Omega}{4\pi} \frac{r}{1 \text{ kpc}} \frac{N_{\text{HI}}}{10^{21} \text{ cm}^{-2}} \left(\frac{v}{350 \text{ km/s}} \right)^3, \quad (4)$$

where C_f is the covering fraction and Ω the opening solid angle in which the gas is outflowing from a radius r .

The energetic quantities defined above are listed in Table 14. The conversion from the kinetic energies to the kinetic luminosities are done via a timescale defined with the radius r and the outflow velocity (or velocity dispersion). The bulk (radial) HI kinetic luminosities and energy loss rates are larger than the turbulent (velocity dispersion only) kinetic luminosities, except for OQ 208. The size of the OQ 208 radio source is small and the HI absorption spectrum exhibits three broad components, which makes the identification of the outflow component difficult. The bulk HI kinetic luminosities repre-

Table 13
Ionized gas kinematics: fit results for mid-IR lines with broad wings

Line	Comp.	λ_c [μm]	v_c [km s^{-1}]	obs. FWHM w_m [km s^{-1}]	int. FWHM w_i [km s^{-1}]	Flux [$10^{-17} \text{ W m}^{-2}$]
3C 236						
[NeII]	n	12.792	-507 ± 33	981 ± 96	844 ± 82	0.55 ± 0.04
[NeII]	b	12.796	-424 ± 121	2172 ± 201	2114 ± 195	0.38 ± 0.03
3C 293						
[NeII]	n	12.818	98 ± 26	779 ± 85	597 ± 65	2.66 ± 0.19
[NeII]	b	12.835	494 ± 51	2338 ± 215	2284 ± 209	1.91 ± 0.16
3C 459						
[NeII]	n	12.824	227 ± 21	804 ± 86	630 ± 67	2.50 ± 0.18
[NeII]	b	12.797	-372 ± 89	1721 ± 163	1647 ± 155	0.80 ± 0.06
4C 12.50						
[NeII]	n	12.810	-88 ± 15	786 ± 85	606 ± 65	3.35 ± 0.24
[NeII]	b	12.779	-812 ± 99	2097 ± 194	2037 ± 189	2.46 ± 0.20
PKS 1549-79						
[NeII]	n	12.814	-5 ± 12	793 ± 83	616 ± 66	1.86 ± 0.13
[NeII]	b	12.775	-906 ± 131	885 ± 142	730 ± 82	0.48 ± 0.04

Note. — Results from a two-component Gaussian decomposition of the [NeII] $12.8\mu\text{m}$ emission line profiles into narrow (n) and broad (b) components. λ_c is the central wavelength of the component and corresponds to a velocity shift v_c of the component with respect to systemic velocity. The statistical error on the velocity shift does not include corrections for the uncertainty in the wavelength calibration, which is 1/5 of a resolution element (100 km s^{-1}). w_m (respectively w_i) is the observed (resp. intrinsic) FWHM before (resp. after) removal of the instrumental profile in quadrature (see sect. 5.1 for details).

Table 14
HI gas kinematics and energetics: broad HI component associated with the neutral outflow

Object	FWHM ^a [km s^{-1}]	Velocity ^b [km s^{-1}]	timescale ^c [yrs]	τ^d	$E_{\text{kin}}^{(\text{turb}) \text{ e}}$ [Joules]	$E_{\text{kin}}^{(\text{bulk}) \text{ f}}$ [Joules]	$L_{\text{kin}}^{(\text{turb}) \text{ g}}$ [L_{\odot}]	$L_{\text{kin}}^{(\text{bulk}) \text{ h}}$ [L_{\odot}]	$\dot{E}(\text{HI})^i$ [L_{\odot}]
3C 236	932	29367	6.5E05	0.0033	5.8E49	2.5E50	7.2E09	1.6E10	2.0E10
3C 293	852	13156	2.0E06	0.0038	3.9E49	3.9E50	1.6E09	1.1E10	1.4E10
3C 305	689	12402	3.9E06	0.0023	1.2E49	3.9E50	2.5E08	1.2E10	5.9E08
3C 459	411	65934	3.3E06	0.0005	1.6E48	1.2E50	4.1E07	4.0E09	3.8E08
4C 12.50	970	36617	3.3E05	0.0017	5.1E48	2.7E49	1.3E09	5.7E09	2.1E09
IC 5063	133	2785	1.1E06	0.0120	2.3E48	1.4E50	1.7E08	8.2E09	3.2E09
OQ 208	482	22568	1.6E04	0.0057	5.0E48	2.0E47	2.5E10	6.5E08	3.4E08
PKS 1549-79	329	45553	3.9E06	0.0200	5.9E48	3.3E51	1.2E08	1.0E11	1.2E10

^a Full width at half maximum of the broad HI component (fitted with a Gaussian).

^b Central velocity of the broad HI component.

^c Outflow timescale derived from the radius r and the outflow velocity.

^d Optical depth of the broad HI component for each velocity components.

^e Turbulent kinetic energy computed from $3/2M(\text{HI})\sigma^2$.

^f Bulk kinetic energy computed by integrating the HI profile (see sect. 5.4 for details).

^g Turbulent kinetic luminosity.

^h Bulk HI kinetic luminosity computed from Eq. 3

ⁱ HI kinetic energy loss rate computed from Eq. 4

sent about a few percent of the Eddington luminosities. This is two orders of magnitude larger than the ionized outflow kinetic power (Holt et al. 2006; Morganti et al. 2007, 2010). We will further discuss these results in sect. 6.2 when examining the transfer of kinetic energy from the jet to the HI and H₂ gas.

5.5. Comparison of the multiphase gas kinematics

In Figure 5, we compare the measured FWHM of the H₂ S(1) and [NeII] $\lambda 12.8\mu\text{m}$ lines. Except for IC 5063 and OQ 208, the [NeII] is systematically broader, by a factor of 40%, than the $17\mu\text{m}$ H₂ S(1) line. This is also the case for the other ionic fine-structure lines: *the velocity dispersion of the ionized gas is generally larger than that of the warm H₂ gas.*

Figure 6 compares the kinematics of the ionized, atomic and warm H₂ gas. In 3C 236, 3C 293, 3C 305, 3C 459, 4C12.50 and PKS 1549-79, the blue-shifted, broad HI ab-

sorption profile matches the blue wing of the [NeII] $\lambda 12.8\mu\text{m}$ line. The ionized and atomic gas are well coupled dynamically and outflowing at comparable velocities. Most of these galaxies are also known to exhibit outflows from optical spectroscopy: blue-shifted 5007 Å [OIII] line emission have been reported in 3C 293 (Emonts et al. 2005), 3C 305 (Morganti et al. 2005b), IC 5063 (Morganti et al. 2007), PKS 1549-79 (Tadhunter et al. 2001; Holt et al. 2008), 4C 12.50 (Holt et al. 2003, 2008) and 3C 459 (Holt et al. 2008). For these three targets, the [OIII] velocity widths and shifts with respect to the systemic velocity are very close to our measurements of the [NeII] $\lambda 12.8\mu\text{m}$ line. Interestingly, in PKS 1549-79, the [NeV] $\lambda 14.3\mu\text{m}$ line is blueshifted by 500–700 km s^{-1} , at the position of the [NeII] and [NeIII] blue wings. This increase of blueshift with increasing ionization has been observed in ULIRGs (Spoon & Holt 2009), and

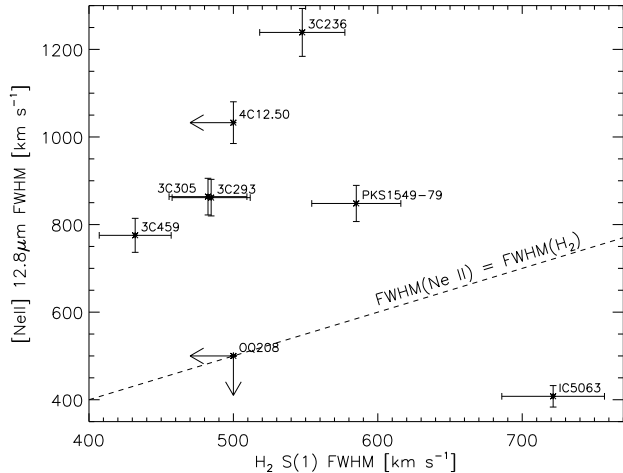


Figure 5. [NeII] λ 12.8 μ m versus H₂ S(1) 17 μ m linewidths (FWHM in km s⁻¹) measured from the *Spitzer* IRS spectra with the high-resolution module (w_m in sect. 5.1). The linewidths are intrinsic, i.e. they have been corrected for the instrumental Gaussian profile.

suggests that the outflow speed decreases with distance to the central ionizing source.

On the other hand, in general, the kinematics of the warm H₂ gas does not follow that of the ionized or atomic gas. In the cases where a blue wing is tentatively detected on the H₂ S(1) line (for 4C 12.50, 3C 459 and PKS 1549-79), the velocity extent of this H₂ wing is smaller than that of the [NeII] line. If some of the H₂ gas is entrained in the flow, its velocity is at least a factor of 2 to 3 smaller than that of the ionized and atomic gas, based on the comparison between the velocity extent of the blue-shifted H₂ S(1) signal, and the one observed for the optical and mid-IR ionized gas lines. Note that the broad molecular line – e.g. CO(1-0)– components detected in composite sources like Mrk 231 are at a 1–5% level of the peak line flux. The limited sensitivity and spectral resolution of the *Spitzer* IRS do not allow us to securely detect such broad wings in the H₂ lines at comparable levels. In addition, if the molecular gas in these galaxies lies in a very turbulent rotating disk (as confirmed by our VLT/SINFONI observations of 3C 326, Nesvadba et al. 2011a), H₂ line wings in spectra integrated over the whole galaxy could be difficult to identify on top of the fast rotation-velocity field.

6. DISCUSSION

6.1. Which dominant mechanism powers the H₂ emission?

Following Ogle et al. (2010), we use the H₂ to PAH luminosity ratio, plotted on Figure 7, to investigate the contribution of UV photons to the total heating of the H₂ gas. In “normal” star-forming galaxies and dwarfs, the tight correlation between the H₂ and PAH luminosities, and the correspondence of the H₂-to-PAH luminosity ratio with PDR models, suggest that most of the H₂ line emission is powered by stellar UV photons (e.g. Rigopoulou et al. 2002; Higdon et al. 2006; Roussel et al. 2007). Strikingly, all of the HI-outflow radio-galaxies have a $L(\text{H}_2)/L(\text{PAH}7.7)$ ratio larger (by at least a factor of 4) than the median value observed for star-forming galaxies (0.0086 for the SINGS galaxies, Roussel et al. 2007). These H₂-bright galaxies fall in the MOHEGs (molecular hydrogen emission galaxies) category (Ogle et al. 2010), defined as $L(\text{H}_2 \text{ S}(0) - \text{S}(3))/L(\text{PAH}7.7) > 0.04$. Using the Meudon PDR code (Le Petit et al. 2006),

we computed the H₂ S(0)-S(3) to PAH 7.7 μ m flux ratio as a function of the $G_{\text{UV}}/n_{\text{H}}$, where G_{UV} is the intensity of the UV radiation field (in Habing units) illuminating a slab of gas of hydrogen density n_{H} . The H₂-to-PAH ratio is high for small values of $G_{\text{UV}}/n_{\text{H}}$. Exploring densities from $n_{\text{H}} = 10^2$ to 10^4 cm⁻³ and $G_{\text{UV}} = 1 - 10^4$, we find a maximum H₂-to-PAH flux ratio of 4×10^{-2} , which is in agreement with the Kaufman et al. (2006) models. This value is precisely the limit chosen empirically by Ogle et al. (2010) to define MOHEGs. All of the HI-outflow radio-galaxies have $L(\text{H}_2)/L(\text{PAH}7.7) > 0.04$ (see Figure 7), showing that their H₂ emission cannot be accounted only by UV heating.

Interestingly enough, Figure 7 shows that the sources having the largest H₂ to PAH luminosity ratio have moderate IR luminosities ($L_{24\mu\text{m}} \approx 10^9 L_{\odot}$) and are jet-dominated, suggesting that the jet plays an important role in powering the H₂ emission. At larger IR luminosities, the sources become dominated by star formation, hence the more moderate H₂ to PAH ratios. We do not find any extreme H₂ to PAH luminosity ratios (> 1) at large IR luminosities ($L_{24\mu\text{m}} \gtrsim 10^{11} L_{\odot}$). This may be due to the fact that all of these sources are at low ($\lesssim 0.3$) redshifts, so the most luminous quasars are not included in this sample. We note that the predominately radio-quiet Higdon et al. (2006) sample of ULIRGs ($0.02 < z < 0.93$) and the Schweitzer et al. (2006) sample of QSOs ($z < 0.3$) have H₂ to PAH luminosity ratios significantly higher than the SINGS star-forming galaxies. Although their H₂ to PAH luminosity ratios are compatible with the range of ratios predicted by PDR models, other studies (based on extinction or H₂-to-CO line ratios), suggest that additional sources of H₂ excitation (other than UV photon heating) are required to explain the H₂ emission (e.g. shocks, see Zakamska 2010; Fiolet et al. 2010).

AGN X-ray heating is potentially a source of H₂ excitation (e.g. Maloney et al. 1996). Assuming a characteristic H₂ gas temperature of 200 K and that all the X-ray flux from the AGN is absorbed by the molecular gas, Ogle et al. (2010) estimated that the maximum H₂-to-X-ray luminosity ratio is of the order of $L(\text{H}_2 \text{ 0-0S}(0) - \text{S}(3))/L_{\text{X}}(2 - 10 \text{ keV}) < 0.01$. We use the c08.01 version of the CLOUDY code, last described by Ferland et al. (1998), to compute this ratio for a cloud of density $n_{\text{H}} = 10^4$ cm⁻³ and a total ionizing photon luminosity corresponding to $L_{\text{X}}(2 - 10 \text{ keV}) = 10^{43}$ erg s⁻¹, which is the average X-ray luminosity measured for our sample. The covering and filling factors are set to unity. For this set of parameters we find $L(\text{H}_2 \text{ 0-0S}(0) - \text{S}(3))/L_{\text{X}}(2 - 10 \text{ keV}) = 7 \times 10^{-3}$, which is in reasonable agreement with the upper limit of 0.01 given above. All HI-outflow radio-galaxies that have X-ray measurements have an observed H₂-to-X-ray flux ratio above that limit (see last column of Table 1), which shows that the X-ray heating cannot be the dominant powering source of the H₂ emission in HI-outflow radio MOHEGs, except perhaps in IC 5063, where the H₂-to-X-ray luminosity ratio is close to 0.01.

Another source of heating for the warm H₂ gas is cosmic rays, as proposed by Ferland et al. (2008) to explain the mid-IR H₂ emission observed from the H α -emitting filament in the Perseus A cool-core cluster (Johnstone et al. 2007). Following, the discussion by Ogle et al. (2010), we find the observed H₂ S(0)-S(3) line cooling (i.e. the H₂ luminosity per H₂ molecule, using the modelled H₂ masses given in Table 6) could be balanced by cosmic ray heating if the cosmic ray ionization rate (per H) is $\zeta_{\text{H}} = 2 \times 10^{-14} - 3 \times 10^{-13}$ s⁻¹,

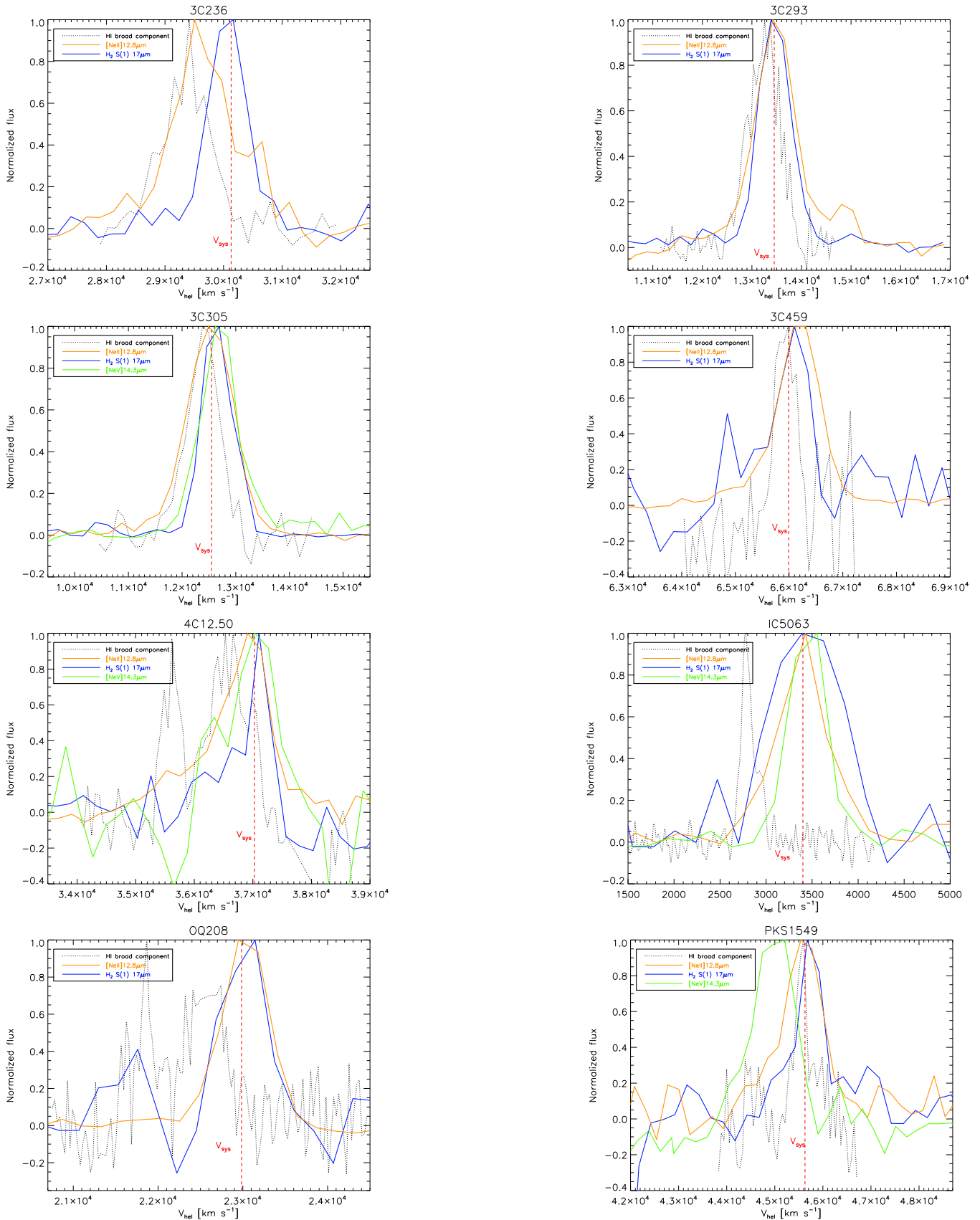


Figure 6. Comparison of the normalized HI absorption (data from Morganti et al. 2005b) (shown on a positive scale) and the *Spitzer* IRS H_2 S(1), [NeII] $\lambda 12.8 \mu\text{m}$ and [NeV] $\lambda 14.3 \mu\text{m}$ (when detected) emission profiles. The dotted black line is the shallower broad HI component associated with the outflowing gas, after removal of the deep, narrower absorption peak. The optical systemic velocity is indicated by a vertical red dashed line. For clarity, the HI spectra of 3C 236, 3C 293, 3C 305, 3C 459 and 4C 12.50 (respectively IC 5063, OQ 208 and PKS 1549-79) have been smoothed to a resolution of $\approx 125 \text{ km s}^{-1}$, (resp. $\approx 30 \text{ km s}^{-1}$). Note that for the *Spitzer* profiles shown here, no correction for instrumental broadening has been applied.

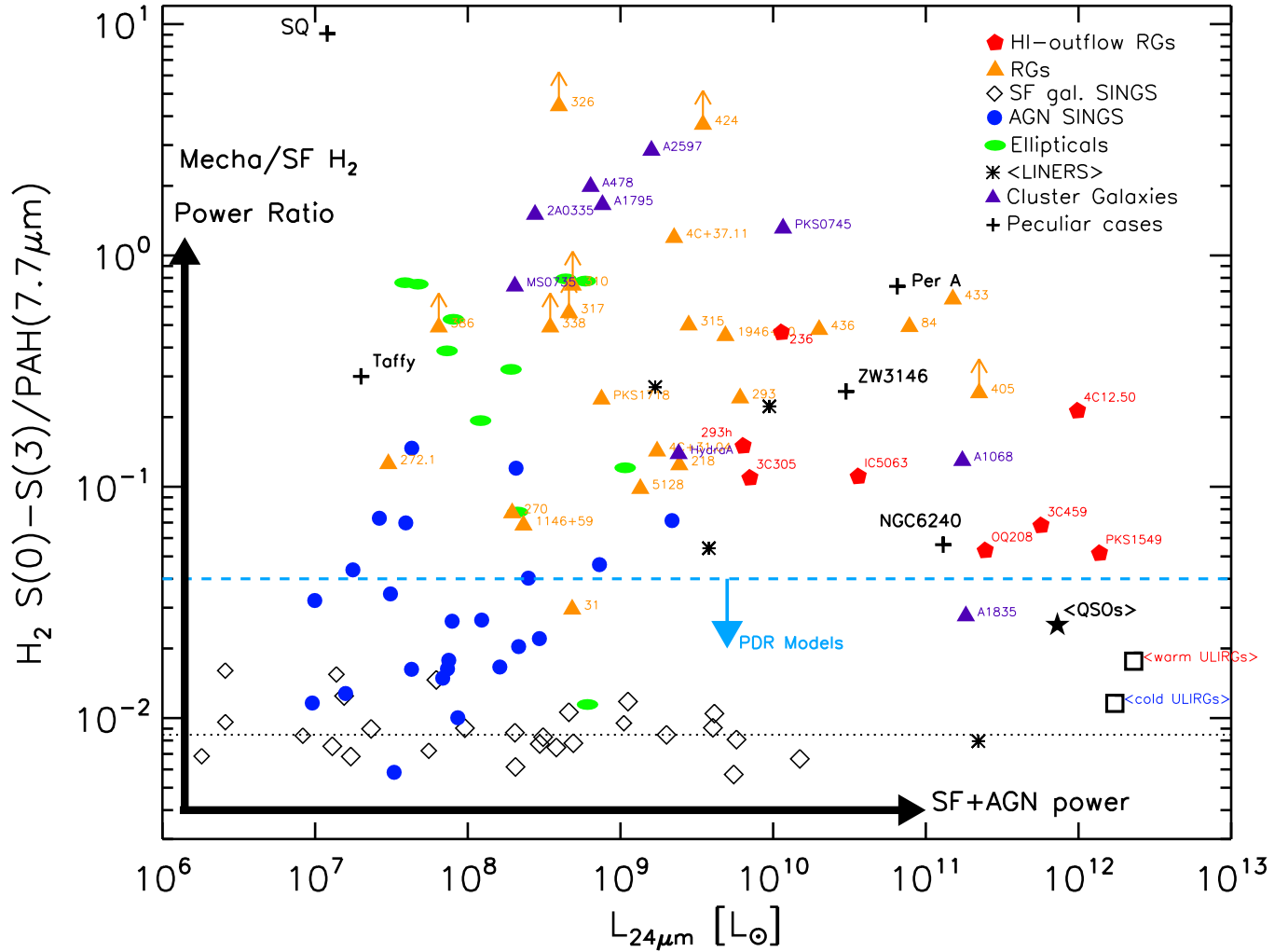


Figure 7. Ratio of the mid-IR H_2 line luminosities (summed over $S(0)$ to $S(3)$) to the PAH $7.7\mu\text{m}$ emission vs. narrow-band $24\mu\text{m}$ continuum luminosity. This ratio indicates the relative contribution of mechanical heating (shocks) and star-formation (SF) power. The red pentagons are the nearby radio galaxies with fast ($>1000\text{ km/s}$) HI outflows. The orange triangles are the H_2 -bright radio-galaxies presented by Ogle et al. (2010), augmented by the compact symmetric objects observed by Willett et al. (2010). The green ellipses are elliptical galaxies from the Kaneda et al. (2008) sample. The purple triangles are the H_2 -bright cool-core galaxy clusters from Donahue et al. (2011). These H_2 -luminous galaxies stand out above SF and AGN galaxies from the SINGS survey (open diamonds and blue circles; data from Roussel et al. 2007). The black dotted line shows the median value of the H_2 -to-PAH luminosity ratio for the SINGS SF galaxies. The H_2 emission in these sources cannot be accounted for by UV or X-ray photon heating. The blue dashed line shows the upper limit given by the Meudon PDR models (Le Petit et al. 2006) obtained for $n_{\text{H}} = 10^4\text{ cm}^{-3}$ and $G_{\text{UV}} = 10$. For comparison, a few other types of H_2 -luminous galaxies are shown (black crosses): the Stephan's Quintet (SQ) and Taffy galaxy collisions (data from Cluver et al. 2010, and Peterson et al., sub.), ZW 3146 (Egami et al. 2006) and Perseus A (Johnstone et al. 2007) clusters, and the NGC 6240 merger (Armus et al. 2006). The black squares indicate averaged values for the Higdon et al. (2006) sample of ULIRGs. The black star is an averaged value of the Schweitzer et al. (2006) sample of QSOs.

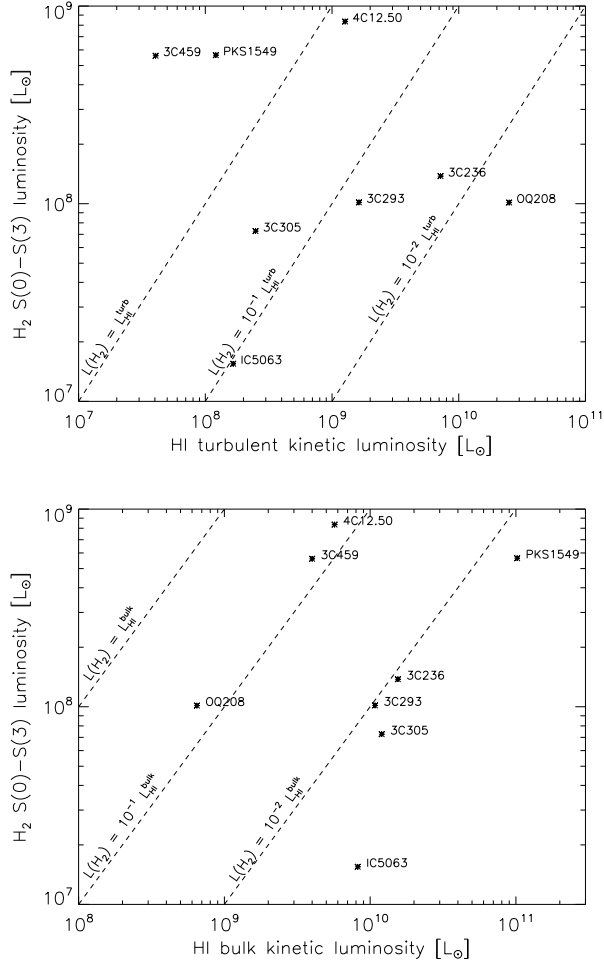


Figure 8. *Top:* H_2 luminosity (summed over the S(0)-S(3) lines) against the HI turbulent kinetic luminosity, derived from the linewidth of the broad HI absorption component, associated with the outflowing gas. *Bottom:* H_2 luminosity as a function of the bulk kinetic luminosity of the HI gas entrained in the flow.

which is $10^3 - 10^4$ times higher than the standard Galactic rate ($\zeta_H = 2.5 \times 10^{-17} \text{ s}^{-1}$, Williams et al. 1998). This would require a cosmic ray pressure 1–10 times higher than the thermal pressure of the warm H_2 gas ($\approx 10^7 \text{ K cm}^{-3}$). Although we cannot exclude it for some of our sources, in the most extreme cases (3C 305, 3C 459, PKS 1549-79) that require the highest ionization rates, it is unlikely that such a departure from the equipartition of energy can be supported on galactic scales.

Ogle et al. (2010) and Nesvadba et al. (2010) argued that the dissipation of the kinetic energy of the radio jet is the most probable source to power the H_2 emission in radio MOHEGs. The fact that *all* the radio sources studied here have bright H_2 emission reinforces the idea that the radio jet, which drives the HI outflow, is also responsible for the shock excitation of the warm H_2 gas. As in 3C 326 (Ogle et al. 2007; Nesvadba et al. 2010), all HI-outflow radio MOHEGs in our sample have jet kinetic powers that exceed the observed H_2 luminosity (see Table 2) and the HI turbulent and bulk kinetic luminosities (see Table 14). The jet provides a huge reservoir of mechanical energy that can be dissipated over timescales of the order of 10^8 yrs, perhaps exceeding the jet lifetime (Nesvadba et al. 2010). Since the cooling time of the warm H_2

gas ($\approx 10^4$ yr) is much shorter than the dynamical timescales of the injection of mechanical energy ($\approx 10^7$ yr), the large masses of warm H_2 gas requires that the gas is repeatedly heated. *Spitzer* H_2 observations thus imply an energy cascade converting bulk kinetic energy of the multi-phase ISM to turbulent motions of much smaller amplitude within molecular gas (Guillard et al. 2009). This is what motivated us to model the observed H_2 line fluxes with shock models (sect. 4.1). The turbulent heating of the molecular gas in powerful AGN is also suggested by observations of highly excited CO lines (e.g. Papadopoulos et al. 2010).

6.2. Efficiency of the transfer from the jet kinetic energy to the HI and H_2 gas

Two main mechanisms may be responsible for driving the observed outflow of HI and ionized gas: the radiation pressure from the AGN (or the starburst if present), or the mechanical impact of the radio source. For the sources studied here, based on the spatial correspondence of the HI broad absorption, optical outflowing component, and an off-nucleus bright spot in the radio jet for some of the sources, we favour the second mechanism. Outflows are most likely driven by the interaction between the expanding radio jets and the ionized/atomic gaseous medium enshrouding the central regions (e.g. Emonts et al. 2005). This may also be the case in even more powerful, high-redshift quasars (Nesvadba et al. 2011b; Polletta et al. 2011) and high-redshift radio galaxies (Humphrey et al. 2006).

The details of the physics that govern the energy transfer from the radio jet to the molecular gas are not yet understood. Being collimated, the jet itself cannot affect a significant fraction of the volume of the ISM of the host galaxy. Instead, the expanding cocoon of hot and tenuous gas inflated by the jet (e.g. Begelman & Cioffi 1989) could transfer part of its kinetic energy to the molecular gas by driving shocks into the dense clouds or/and by turbulent mixing between hot and cold gas, similarly to the process proposed by Guillard et al. (2009) to explain the powerful H_2 emission from the Stephan’s Quintet galaxy collision. It also possible that part of the bulk kinetic energy of the outflowing HI gas is transferred to the molecular phase through shocks. The top (respectively bottom) panel of Figure 8 compares the H_2 luminosity to the turbulent (resp. bulk) HI kinetic luminosity. In all sources, the bulk HI kinetic luminosity exceeds by more than one order of magnitude the observed H_2 luminosities. The dissipation of a small fraction ($< 10\%$) of this kinetic energy in the molecular gas could power the H_2 emission.

Numerical simulations of the impact of jets on galaxy evolution stress the importance of considering the multi-phase nature of the host galaxy ISM (e.g. Sutherland & Bicknell 2007). Wagner & Bicknell (2011) showed that the efficiency of transfer of kinetic energy and momentum from the jet to the dense ($n_H > 10^2 \text{ cm}^{-3}$) gas can be high (10-70%), with the momentum flux of the clouds exceeding that of the jet. However, the mid-IR *IRS* spectroscopy of the H_2 rotational lines presented in this paper indicates that most of the molecular gas does not share the kinematics of the outflowing atomic and ionized gas. If most of the H_2 gas was in the outflow, we would have observed blue-shifted H_2 lines, similar to the ionized gas lines. This suggests that the dynamical coupling between the molecular gas and the more tenuous outflowing gas is weak, probably because of the high density contrast between these phases. For density contrast of 10^4 , it

takes $\approx 4 \times 10^8$ yrs to accelerate a 10 pc cloud up to a velocity of 500 km s^{-1} (e.g. Klein et al. 1994), which is likely to be longer than the jet lifetime. If some H_2 gas is effectively outflowing, the wind would remove this gas gradually over an AGN lifetime. It is very unlikely that the entire mass of the molecular disk would be entrained in the wind. Thus the fraction of the molecular gas expelled from these galaxies could be small, which does not fit with the current assumptions made in the cosmological galaxy evolution models that assumes that AGN feedback sweep up most of the gas during the epochs of strong star-formation (e.g. Hopkins et al. 2006; Narayanan et al. 2008).

The current numerical simulations show a very efficient transfer of momentum essentially because the dense ($n_{\text{H}} > 1 \text{ cm}^{-3}$, $T = 10^4 \text{ K}$) gas cools very fast. These calculations do not include the turbulent cascade and dissipation of the kinetic energy due to the supersonic turbulence within the dense gas phase, which would make the gas cooling longer, and therefore the dynamical coupling less efficient. The dynamical coupling would be much more efficient if a significant fraction of the warm H_2 gas is formed *in situ*, i.e. in the outflow, from shocked HI gas. On the contrary, our data suggest that the bulk of the warm H_2 mass is difficult to entrain in the outflow, and is rather perhaps settled in the galactic disk. A similar conclusion is reached based on near-IR IFU observations of nearby Seyfert galaxies (Storchi-Bergmann et al. 2009; Riffel & Storchi-Bergmann 2011), where the H_2 gas is concentrated in the galactic plane (with a velocity structure consistent with a rotating disk), whereas the ionized gas is mostly distributed along the outflowing cone.

On the other hand, in some of the sources studied here, the H_2 lines are broad, showing that the H_2 gas is very turbulent. This suggests that the molecular gas is heated by the dissipation of supersonic turbulence, which can prevent it from being gravitationally bound (and thus from forming stars), rather than expelled from the galaxy. In some cases, these turbulent motions are unlikely to be rotation-supported. Assuming the galaxies are pressure-supported with an isothermal mass profile, we derived the escape velocities, v_{esc} , from the stellar masses: $v_{\text{esc}} = \sqrt{2GM_*/(5r_e)}$. We assume an effective radius of $r_e = 2 \text{ kpc}$. We find escape velocities that range from 70 km s^{-1} (OQ 208) to 330 km s^{-1} (4C 12.50). In all of the sources, the observed H_2 velocity dispersions (up to $\approx 300 \text{ km s}^{-1}$, broader than that observed in nearby Seyferts) are comparable to their escape velocities, except for IC 5063, where $\sigma(\text{H}_2) \approx 3 \times v_{\text{esc}}$. Thus, a fraction of the warm H_2 gas could become unbound and escape from these galaxies because of its high velocity dispersion. However, the fraction of the H_2 S(1) line emission having velocities larger than the escape velocity is small ($\lesssim 10\%$), so it is unlikely that this process would strongly affect and empty the reservoir of molecular gas in these galaxies.

We are complementing the observations presented here with higher resolution spectroscopy of near-IR H_2 lines, interferometric CO line observations, and *Herschel* spectroscopy and photometry, to complete our census of the physical and dynamical state of the molecular gas in these sources. For extended objects, the use of near-IR IFUs is necessary. Hopefully, JWST/MIRI will allow us to probe mid-IR H_2 lines at a much better sensitivity and $5 \times$ better spectral resolution than the *IRS*.

7. CONCLUSIONS AND FINAL REMARKS

We present mid-IR *Spitzer* spectroscopy of 8 nearby radio-galaxies where fast outflows of ionized and atomic gas were detected by previous optical and radio observations. Our main results and conclusions are the following:

- In all of the sources, we detect high equivalent width H_2 line emission from warm (100-5000 K) molecular gas, implying warm H_2 masses ranging from 10^8 to $10^{10} M_{\odot}$. The observed H_2 -to-PAH luminosity ratios are all above the values predicted from photo-ionization models, and we suggest that the H_2 emission is associated with the dissipation of a fraction of the kinetic energy provided by the radio jet.
- In 5 sources (3C 236, 3C 293, 3C 459, 4C 12.50 and PKS 1549-79), we securely detect blue-shifted wings (up to 3000 km s^{-1}) on the [NeII] (and [NeIII] for the highest SNR spectra) that matches remarkably well with the blue-shifted, broad HI absorption associated with the outflow.
- All but one of these sources have resolved and very broad mid-IR rotational H_2 lines with $\text{FWHM} \gtrsim 500 \text{ km s}^{-1}$ (and up to 900 km s^{-1}), compared to only 2% overall amongst the 298 AGN with such spectra in the *Spitzer* archive (Dasyra & Combes 2011). This suggests that the efficiency of kinetic energy deposition into the molecular ISM is higher in radio jet sources than in other types of AGN.
- The kinematics of the warm H_2 gas do not follow that of the ionized or HI gas. The rotational H_2 lines are systemically narrower than the mid-IR ionized gas lines, and do not exhibit asymmetric profiles with blue-shifted wings (except perhaps tentative detections in three targets, 4C 12.50, 3C 459, and PKS 1549-79). We conclude that, although very turbulent, the bulk of the warm H_2 mass is not entrained in the wind.
- We show that UV, X-ray and cosmic ray heating are unlikely to be the dominant source of H_2 excitation. We argue that the dissipation (via supersonic turbulence) of a small fraction ($< 10\%$) of the mechanical energy provided by the radio jet can power the observed emission.

This work is based primarily on observations made with the *Spitzer Space Telescope*, which is operated by the Jet Propulsion Laboratory, California Institute of Technology under a contract with NASA.

This research has made use of the NASA/IPAC Extragalactic Database (NED) which is operated by the Jet Propulsion Laboratory, California Institute of Technology, under contract with the National Aeronautics and Space Administration.

REFERENCES

- Alatalo, K., et al. 2011, *ApJ*, 735, 88
 Alexander, D. M., Smail, I., Bauer, F. E., Chapman, S. C., Blain, A. W., Brandt, W. N., & Ivison, R. J. 2005, *Nature*, 434, 738
 Alexander, T., Sturm, E., Lutz, D., Sternberg, A., Netzer, H., & Genzel, R. 1999, *ApJ*, 512, 204
 Allen, M. G., Groves, B. A., Dopita, M. A., Sutherland, R. S., & Kewley, L. J. 2008, *ApJS*, 178, 20
 Armus, L., et al. 2006, *ApJ*, 640, 204

- Axon, D. J., Capetti, A., Fanti, R., Morganti, R., Robinson, A., & Spencer, R. 2000, *AJ*, 120, 2284
- Bahcall, J. N., & Ekers, R. D. 1969, *ApJ*, 157, 1055
- Begelman, M. C., & Cioffi, D. F. 1989, *ApJ*, 345, L21
- Bernard-Salas, J., et al. 2009, *ApJS*, 184, 230
- Best, P. N., Kaiser, C. R., Heckman, T. M., & Kauffmann, G. 2006, *MNRAS*, 368, L67
- Best, P. N., Kauffmann, G., Heckman, T. M., Brinchmann, J., Charlot, S., Ivezić, Ž., & White, S. D. M. 2005, *MNRAS*, 362, 25
- Cluver, M. E., et al. 2010, *ApJ*, 710, 248
- Crenshaw, D. M., Kraemer, S. B., & George, I. M. 2003, *ARA&A*, 41, 117
- Dasyra, K. M., & Combes, F. 2011, *ApJ*, A&A, 533, L10
- Dasyra, K. M., et al. 2008, *ApJ*, 674, L9
- de Koff, S., et al. 2000, *ApJS*, 129, 33
- Di Matteo, T., Springel, V., & Hernquist, L. 2005, *Nature*, 433, 604
- Dicken, D., et al. 2011, *ArXiv e-prints*
- Donahue, M., de Messières, G. E., O’Connell, R. W., Voit, G. M., Hoffer, A., McNamara, B. R., & Nulsen, P. E. J. 2011, *ApJ*, 732, 40
- Donoso, E., Best, P. N., & Kauffmann, G. 2009, *MNRAS*, 392, 617
- Dopita, M. A., & Sutherland, R. S. 1996, *ApJS*, 102, 161
- Dudik, R. P., Satyapal, S., & Marcu, D. 2009, *ApJ*, 691, 1501
- Egami, E., Rieke, G. H., Fadda, D., & Hines, D. C. 2006, *ApJ*, 652, L21
- Emonts, B. H. C., Morganti, R., Tadhunter, C. N., Oosterloo, T. A., Holt, J., & van der Hulst, J. M. 2005, *MNRAS*, 362, 931
- Evans, A. S., Mazzarella, J. M., Surace, J. A., & Sanders, D. B. 2002, *ApJ*, 580, 749
- Evans, A. S., Sanders, D. B., Surace, J. A., & Mazzarella, J. M. 1999, *ApJ*, 511, 730
- Farrah, D., et al. 2007, *ApJ*, 667, 149
- Ferland, G. J., Fabian, A. C., Hatch, N. A., Johnstone, R. M., Porter, R. L., van Hoof, P. A. M., & Williams, R. J. R. 2008, *MNRAS*, 386, L72
- Ferland, G. J., Korista, K. T., Verner, D. A., Ferguson, J. W., Kingdon, J. B., & Verner, E. M. 1998, *PASP*, 110, 761
- Ferland, G. J., & Netzer, H. 1983, *ApJ*, 264, 105
- Ferrarese, L., & Merritt, D. 2000, *ApJ*, 539, L9
- Feruglio, C., Maiolino, R., Piconcelli, E., Menci, N., Aussel, H., Lamastra, A., & Fiore, F. 2010, *A&A*, 518, L155+
- Fiolet, N., et al. 2010, *A&A*, 524, A33+
- Fischer, J., et al. 2010, *A&A*, 518, L41+
- Flower, D. R., & Pineau Des Forêts, G. 2010, *MNRAS*, 406, 1745
- Groves, B., Dopita, M., & Sutherland, R. 2006, *A&A*, 458, 405
- Guainazzi, M., Siemiginowska, A., Rodriguez-Pascual, P., & Stanghellini, C. 2004, *A&A*, 421, 461
- Guillard, P., Boulanger, F., Pineau Des Forêts, G., & Appleton, P. N. 2009, *A&A*, 502, 515
- Heckman, T. M. 2002, 254, 292
- Heisler, C. A., & Vader, J. P. 1994, *AJ*, 107, 35
- Higdon, S. J. U., Armus, L., Higdon, J. L., Soifer, B. T., & Spoon, H. W. W. 2006, *ApJ*, 648, 323
- Hill, G. J., Goodrich, R. W., & Depoy, D. L. 1996, *ApJ*, 462, 163
- Holt, J., Tadhunter, C., Morganti, R., Bellamy, M., González Delgado, R. M., Tzioumis, A., & Inskip, K. J. 2006, *MNRAS*, 370, 1633
- Holt, J., Tadhunter, C. N., & Morganti, R. 2003, *MNRAS*, 342, 227
- , 2008, *MNRAS*, 387, 639
- Holt, J., Tadhunter, C. N., Morganti, R., & Emonts, B. H. C. 2011, *MNRAS*, 410, 1527
- Hony, S., Van Kerckhoven, C., Peeters, E., Tielens, A. G. G. M., Hudgins, D. M., & Allamandola, L. J. 2001, *A&A*, 370, 1030
- Hopkins, P. F., Hernquist, L., Cox, T. J., Robertson, B., & Springel, V. 2006, *ApJS*, 163, 50
- Houck, J. R., et al. 2004, *ApJS*, 154, 18
- Humphrey, A., Villar-Martín, M., Fosbury, R., Vernet, J., & di Serego Alighieri, S. 2006, *MNRAS*, 369, 1103
- Johnstone, R. M., Hatch, N. A., Ferland, G. J., Fabian, A. C., Crawford, C. S., & Wilman, R. J. 2007, *MNRAS*, 382, 1246
- Kaneda, H., Onaka, T., Sakon, I., Kitayama, T., Okada, Y., & Suzuki, T. 2008, *ApJ*, 684, 270
- Kaufman, M. J., Wolfire, M. G., & Hollenbach, D. J. 2006, *ApJ*, 644, 283
- Klein, R. I., McKee, C. F., & Colella, P. 1994, *ApJ*, 420, 213
- Le Petit, F., Nehmé, C., Le Bourlot, J., & Roueff, E. 2006, *ApJS*, 164, 506
- Lehnert, M. D., Tasse, C., Nesvadba, N. P. H., Best, P. N., & van Driel, W. 2011, *A&A*, 532, L3+
- Lutz, D., Maiolino, R., Spoon, H. W. W., & Moorwood, A. F. M. 2004, *A&A*, 418, 465
- Maloney, P. R., Hollenbach, D. J., & Tielens, A. G. G. M. 1996, *ApJ*, 466, 561
- Marconi, A., & Hunt, L. K. 2003, *ApJ*, 589, L21
- Markwardt, C. B. 2009, in *Astronomical Society of the Pacific Conference Series*, Vol. 411, *Astronomical Society of the Pacific Conference Series*, ed. D. A. Bohlender, D. Durand, & P. Dowler, 251–+
- Marziani, P., Sulentic, J. W., Calvani, M., Perez, E., Moles, M., & Penston, M. V. 1993, *ApJ*, 410, 56
- Massaro, F., et al. 2009, *ApJ*, 692, L123
- Meijerink, R., Spaans, M., & Israel, F. P. 2007, *A&A*, 461, 793
- Morganti, R., Holt, J., Saripalli, L., Oosterloo, T. A., & Tadhunter, C. N. 2007, *A&A*, 476, 735
- Morganti, R., Holt, J., Tadhunter, C., & Oosterloo, T. 2010, in *IAU Symposium*, Vol. 267, *IAU Symposium*, 429–437
- Morganti, R., Oosterloo, T., & Tsvetanov, Z. 1998, *AJ*, 115, 915
- Morganti, R., Oosterloo, T. A., Emonts, B. H. C., van der Hulst, J. M., & Tadhunter, C. N. 2003, *ApJ*, 593, L69
- Morganti, R., Oosterloo, T. A., Tadhunter, C. N., van Moorsel, G., & Emonts, B. 2005a, *A&A*, 439, 521
- Morganti, R., Tadhunter, C. N., & Oosterloo, T. A. 2005b, *A&A*, 444, L9
- Narayanan, D., et al. 2008, *ApJS*, 176, 331
- Nesvadba, N., Boulanger, F., Lehnert, M., Guillard, P., & Salome, P. 2011a, *ArXiv e-prints*
- Nesvadba, N. P. H., Lehnert, M. D., Davies, R. I., Verma, A., & Eisenhauer, F. 2008, *A&A*, 479, 67
- Nesvadba, N. P. H., Lehnert, M. D., Eisenhauer, F., Gilbert, A., Tecza, M., & Abuter, R. 2006, *ApJ*, 650, 693
- Nesvadba, N. P. H., Polletta, M., Lehnert, M. D., Bergeron, J., De Breuck, C., Lagache, G., & Omont, A. 2011b, *MNRAS*, 415, 2359
- Nesvadba, N. P. H., et al. 2010, *A&A*, 521, A65+
- Nilsson, K., Valtonen, M. J., Kotilainen, J., & Jaakkola, T. 1993, *ApJ*, 413, 453
- Ocaña Flaquer, B., Leon, S., Combes, F., & Lim, J. 2010, *A&A*, 518, A9+
- O’Dea, C. P., De Vries, W. H., Worrall, D. M., Baum, S. A., & Koekemoer, A. 2000, *AJ*, 119, 478
- Ogle, P., Antonucci, R., Appleton, P. N., & Whysong, D. 2007, *ApJ*, 668, 699
- Ogle, P., Boulanger, F., Guillard, P., Evans, D. A., Antonucci, R., Appleton, P. N., Nesvadba, N., & Leipski, C. 2010, *ApJ*, 724, 1193
- Oosterloo, T. A., Morganti, R., Tzioumis, A., Reynolds, J., King, E., McCulloch, P., & Tsvetanov, Z. 2000, *AJ*, 119, 2085
- Papadopoulos, P. P., van der Werf, P., Isaak, K., & Xilouris, E. M. 2010, *ApJ*, 715, 775
- Polletta, M., Nesvadba, N. P. H., Neri, R., Omont, A., Berta, S., & Bergeron, J. 2011, *ArXiv e-prints*
- Punsly, B. 2005, *ApJ*, 623, L9
- Reynolds, C., Punsly, B., Kharb, P., O’Dea, C. P., & Wrobel, J. 2009, *ApJ*, 706, 851
- Riffel, R. A., & Storchi-Bergmann, T. 2011, *MNRAS*, 411, 469
- Rigopoulou, D., Kunze, D., Lutz, D., Genzel, R., & Moorwood, A. F. M. 2002, *A&A*, 389, 374
- Roussel, H., et al. 2007, *ApJ*, 669, 959
- Rupke, D. S., Veilleux, S., & Sanders, D. B. 2005, *ApJS*, 160, 115
- Schweitzer, M., et al. 2006, *ApJ*, 649, 79
- Silk, J., & Rees, M. J. 1998, *A&A*, 331, L1
- Smith, J. D. T., et al. 2007, *ApJ*, 656, 770
- Spoon, H. W. W., & Holt, J. 2009, *ApJ*, 702, L42
- Storchi-Bergmann, T., McGregor, P. J., Riffel, R. A., Simões Lopes, R., Beck, T., & Dopita, M. 2009, *MNRAS*, 394, 1148
- Sturm, E., Lutz, D., Verma, A., Netzer, H., Sternberg, A., Moorwood, A. F. M., Oliva, E., & Genzel, R. 2002, *A&A*, 393, 821
- Sturm, E., et al. 2011, *ApJ*, 733, L16+
- Sutherland, R. S., & Bicknell, G. V. 2007, *ApJS*, 173, 37
- Tadhunter, C., Wills, K., Morganti, R., Oosterloo, T., & Dickson, R. 2001, *MNRAS*, 327, 227
- Tadhunter, C., et al. 2011, *MNRAS*, 412, 960
- Thomas, D., Maraston, C., Bender, R., & Mendes de Oliveira, C. 2005, *ApJ*, 621, 673
- Tremaine, S., et al. 2002, *ApJ*, 574, 740
- Veilleux, S., & Osterbrock, D. E. 1987, *ApJS*, 63, 295
- Veilleux, S., Rupke, D. S. N., & Swaters, R. 2009, *ApJ*, 700, L149
- Voit, G. M. 1992, *MNRAS*, 258, 841
- Wagner, A. Y., & Bicknell, G. V. 2011, *ApJ*, 728, 29
- Willet, K. W., Stocke, J. T., Darling, J., & Perlman, E. S. 2010, *ApJ*, 713, 1393
- Williams, J. P., Bergin, E. A., Caselli, P., Myers, P. C., & Plume, R. 1998, *ApJ*, 503, 689
- Xiang, L., Stanghellini, C., Dallacasa, D., & Haiyan, Z. 2002, *A&A*, 385, 768
- Zakamska, N. L. 2010, *Nature*, 465, 60

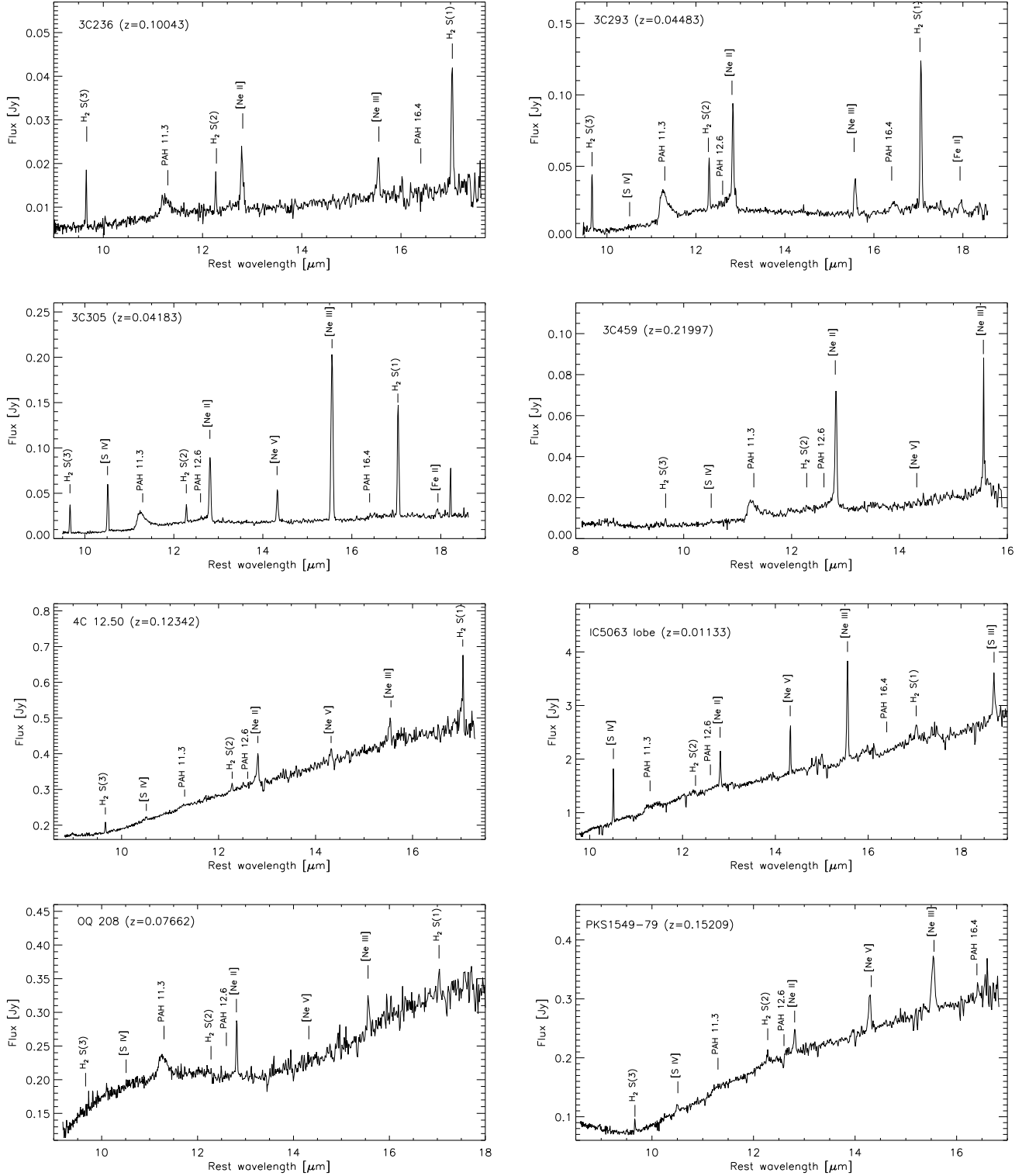


Figure 9. Spitzer IRS high-resolution spectra of the HI-outflow radio galaxies, zoomed on the wavelength coverage of the SH (Short High) module.

Zirbel, E. L., & Baum, S. A. 1998, *ApJS*, 114, 177

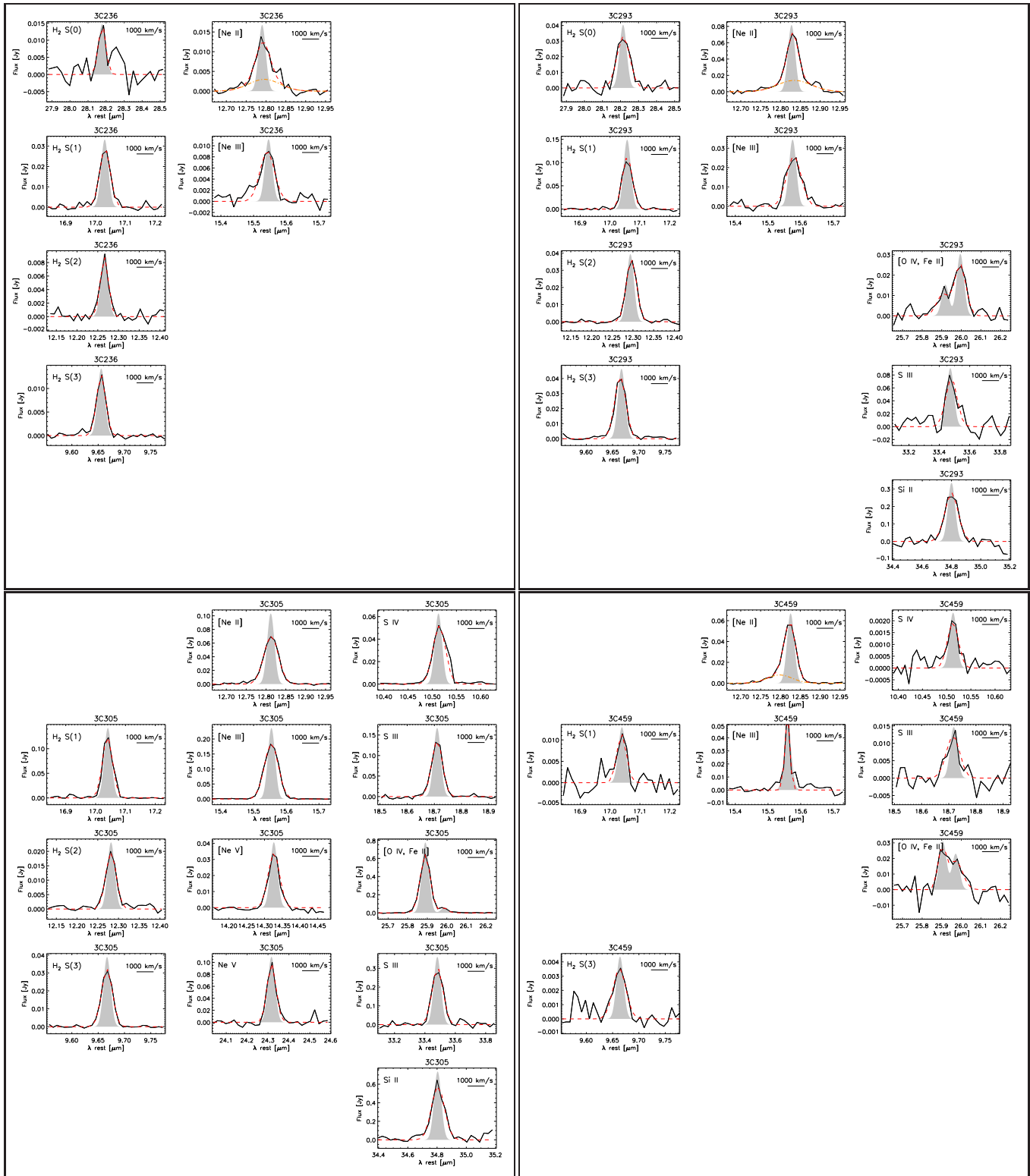


Figure 10. Detected spectral emission lines. The grey area is the *Spitzer* IRS instrumental profile (a Gaussian with a FWHM corresponding to the resolution of the IRS), and the red dashed line is the result of the Gaussian fitting of the line. The [O IV, Fe II] blend profile has been fitted with two Gaussian components when both lines are detected. For lines showing wings, the broad component of the Gaussian decomposition is overplotted (orange dashed-dotted line).

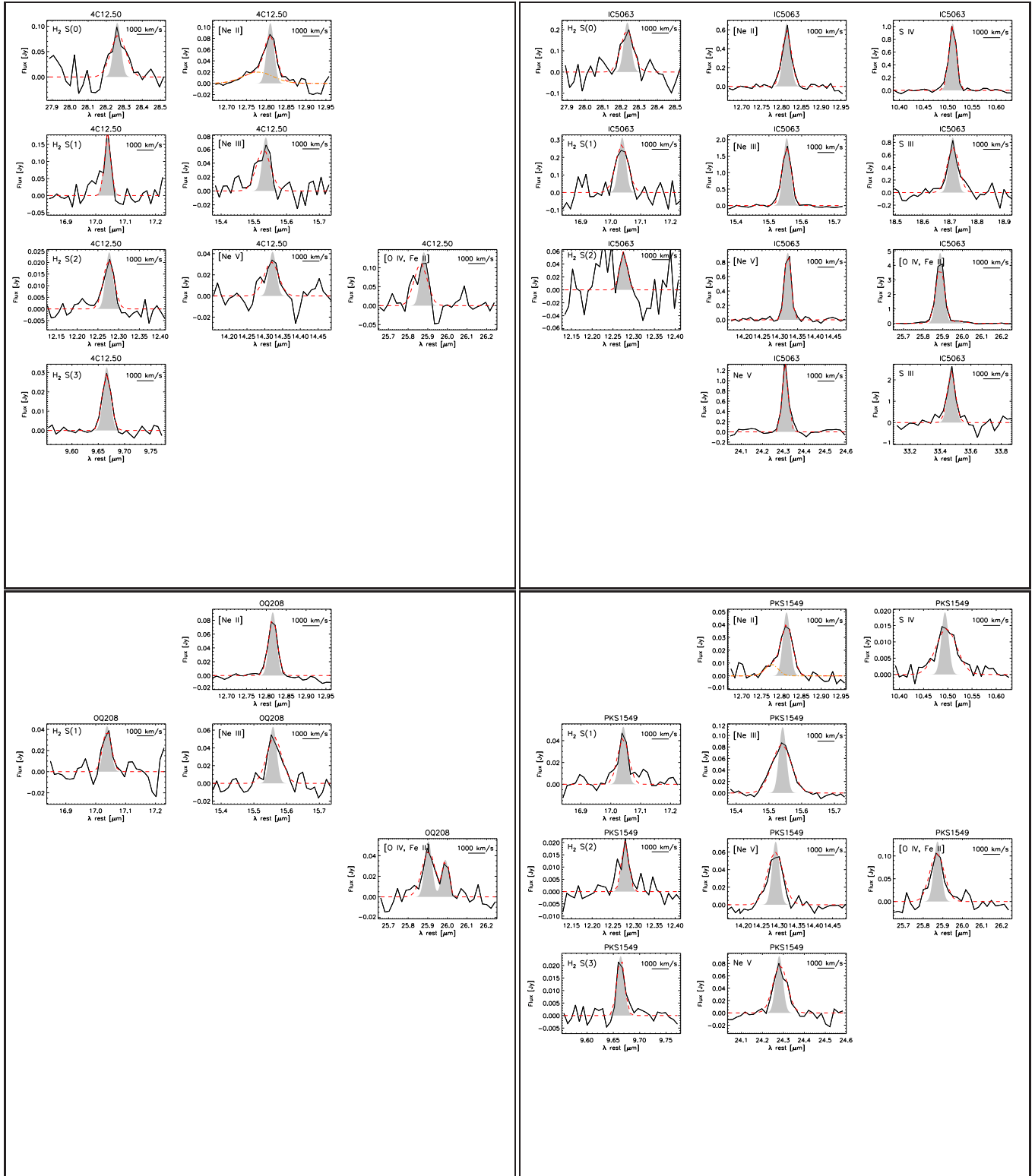


Figure 11. Detected spectral emission lines. The grey area is the *Spitzer* IRS instrumental profile (a Gaussian with a FWHM corresponding to the resolution of the IRS), and the red dashed line is the result of the Gaussian fitting of the line. The [O IV, Fe II] blend profile has been fitted with two Gaussian components when both lines are detected. For lines showing wings, the broad component of the Gaussian decomposition is overplotted (orange dashed-dotted line).

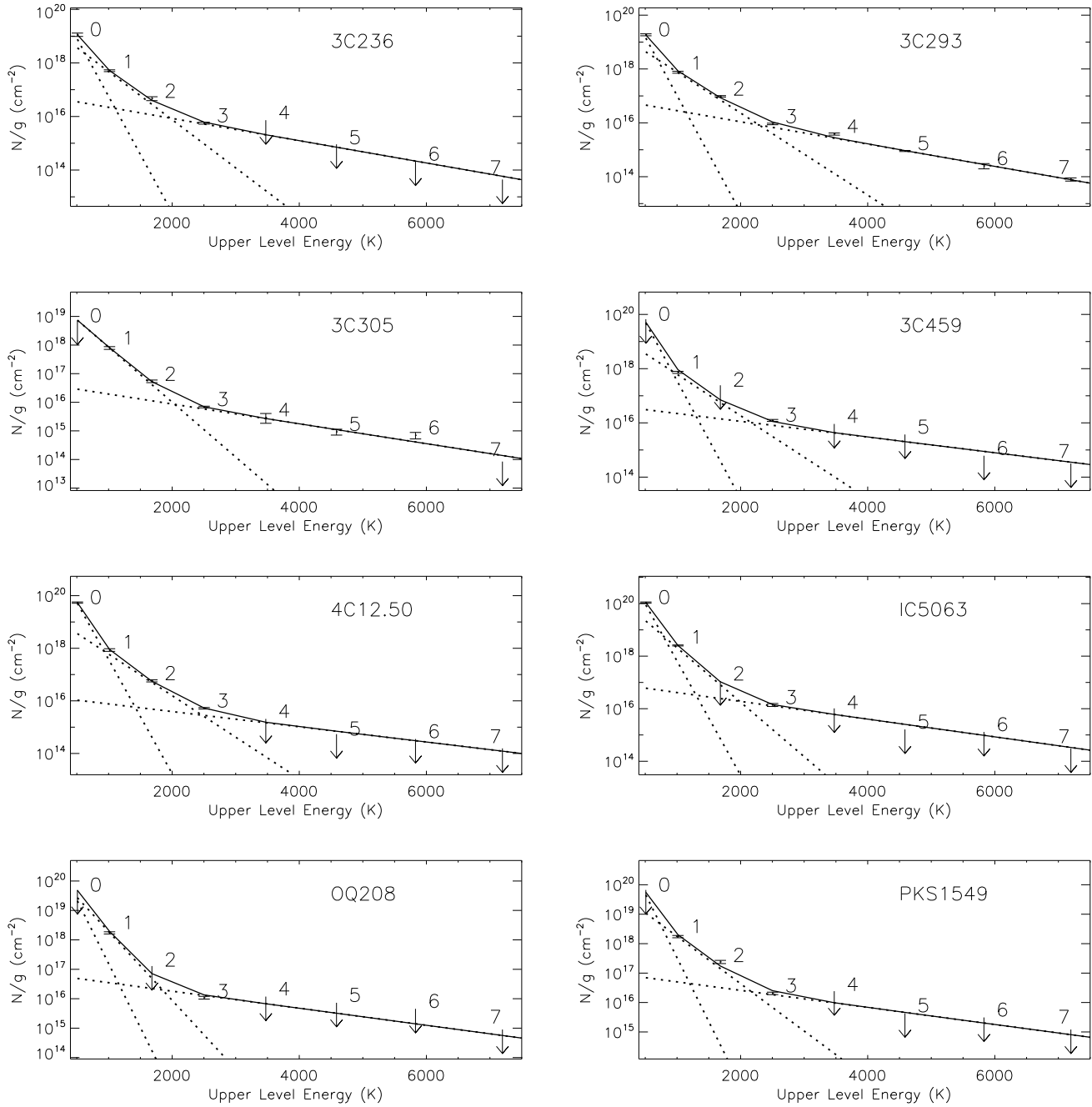


Figure 12. H₂ excitation diagrams with two or three temperature component fits overlaid. The H₂ temperatures, column densities, and masses are listed in Table 5.

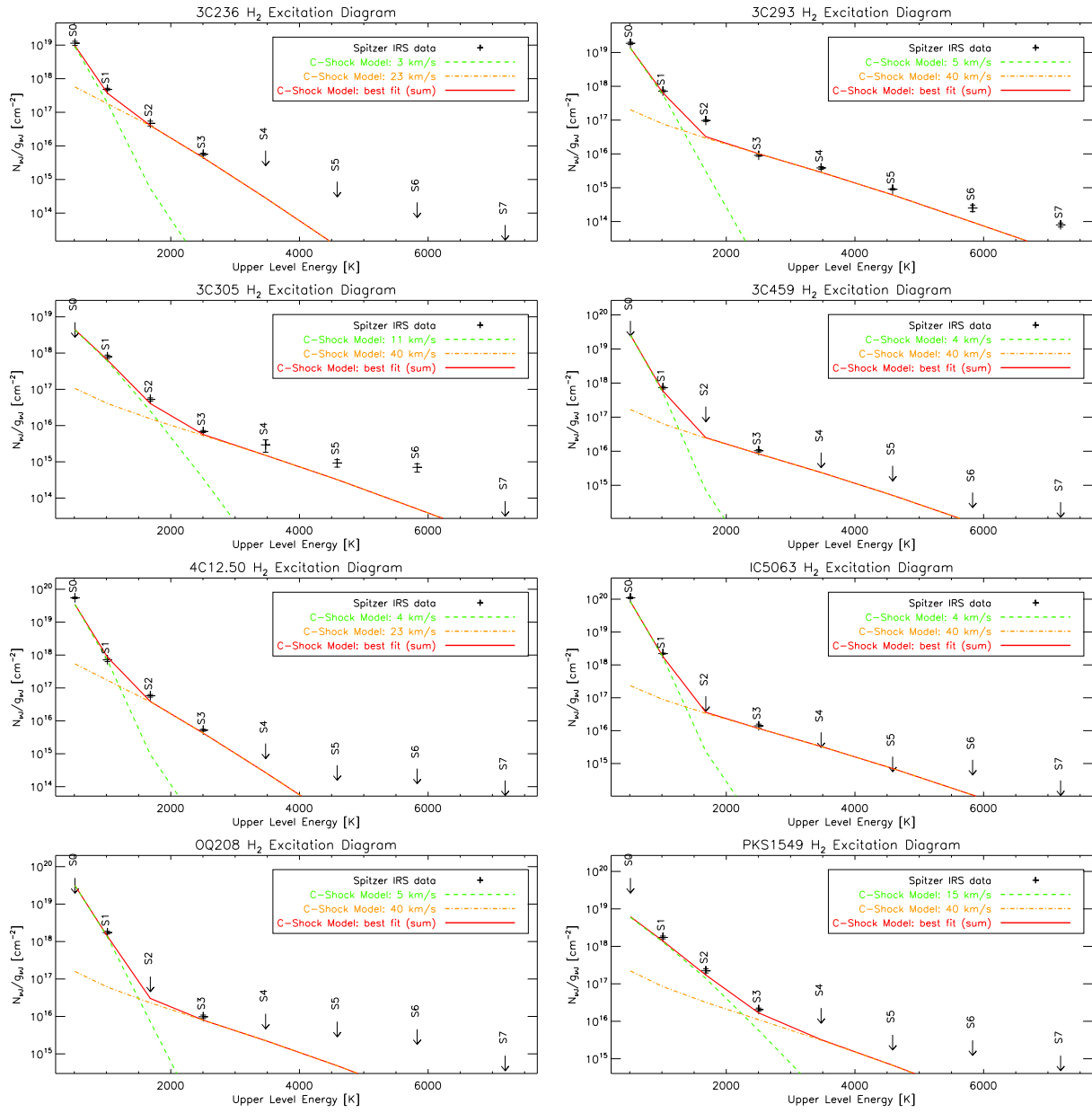


Figure 13. H₂ excitation diagrams fitted with a combination of two C-shock models, for a pre-shock density of $n_{\text{H}} = 10^3 \text{ cm}^{-3}$. The shock model parameters, and H₂ masses are listed in Table 6.

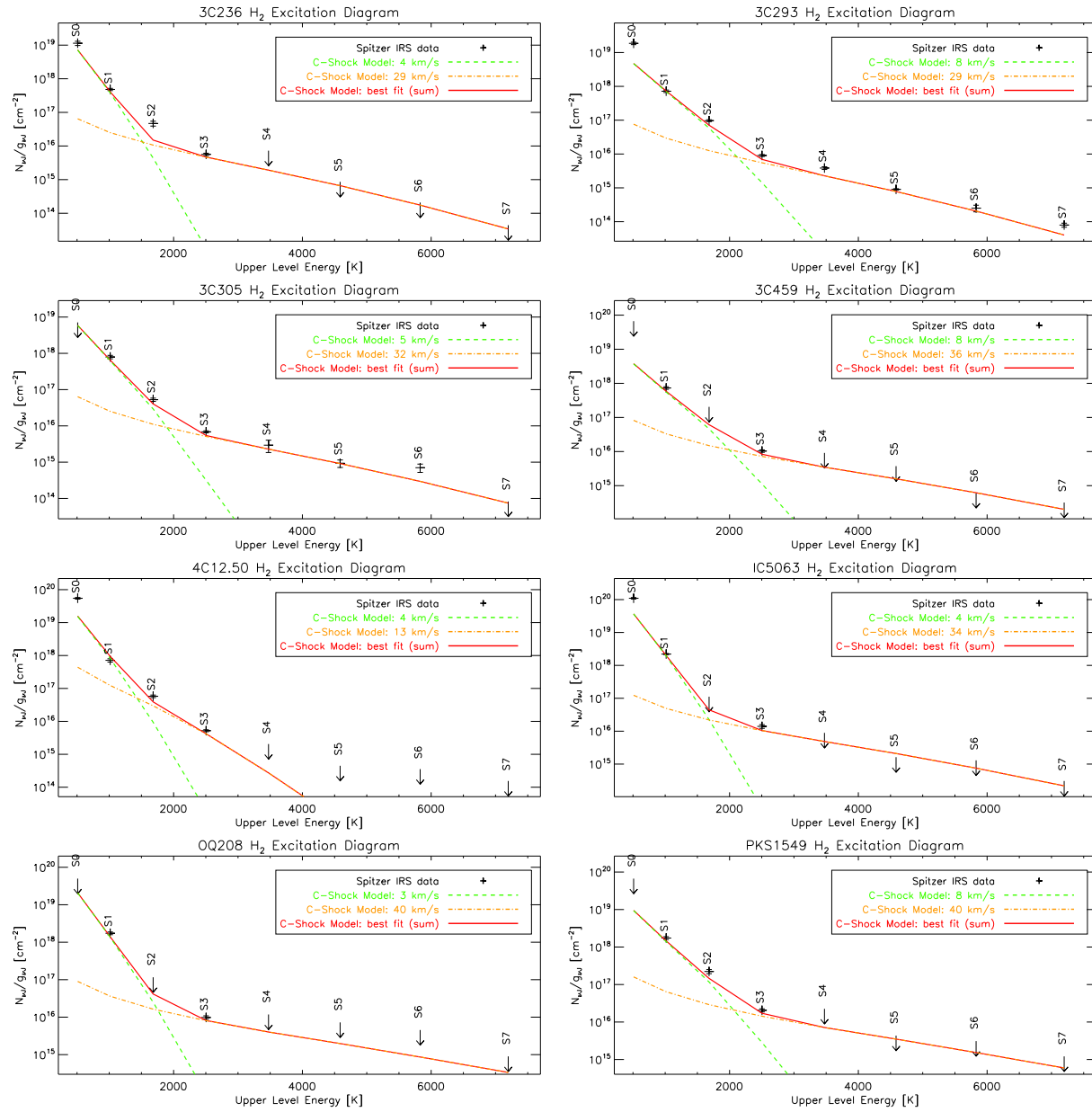


Figure 14. H₂ excitation diagrams fitted with a combination of two C-shock models, for a pre-shock density of $n_{\text{H}} = 10^4 \text{ cm}^{-3}$. The shock model parameters, and H₂ masses are listed in Table 7.

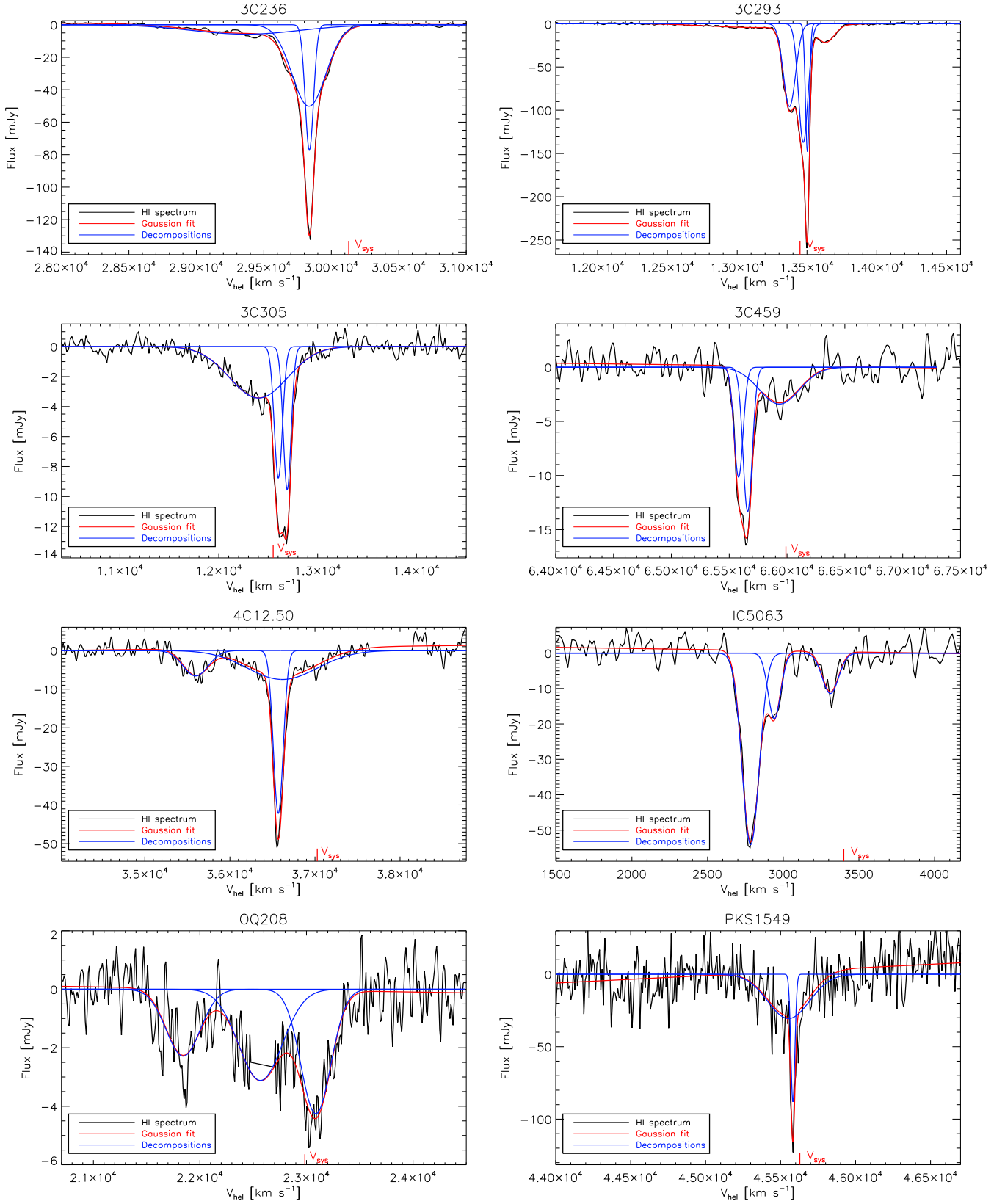


Figure 15. Gaussian decompositions of the HI absorption profiles observed with the Westerbork telescope. The data is from [Morganti et al. \(2005b\)](#), except for 3C 293, where we used more recent observations taken by B. Emonts with the Westerbork telescope.